

ELECTRON CAPTURE SUPERNOVAE FROM CLOSE BINARY SYSTEMS

AREND J.T. POELARENDIS, SCOTT WURTZ, JAMES TARKA, COLE ADAMS AND SPENCER T. HILLS

Wheaton College
Department of Physics and Astronomy
501 College Ave
Wheaton, IL 60187 USA
E-mail: aj.poelarends@wheaton.edu

ABSTRACT

We present the first detailed study of the Electron Capture Supernova Channel (ECSN Channel) for a primary star in a close binary star system. Progenitors of ECSN occupy the lower end of the mass spectrum of supernovae progenitors and are thought to form the transition between white dwarfs progenitors and core collapse progenitors. The mass range for ECSN from close binary systems is thought to be wider than the range for single stars, because of the effects of mass transfer on the helium core. Using the MESA stellar evolution code we explored the parameter space of initial primary masses between $8 M_{\odot}$ and $17 M_{\odot}$, using a large grid of models. We find that the initial primary mass and the mass transfer evolution are important factors in the final fate of stars in this mass range. Mass transfer due to Roche Lobe overflow during and after carbon burning causes the core to cool down so that it avoids neon ignition, even in helium-free cores with masses up to $1.52 M_{\odot}$, which in single stars would ignite neon. If the core is able to contract to high enough densities for electron captures to commence, we find that, for the adopted Ledoux convection criterion, the initial mass range for the primary to evolve into an ECSN is between $13.5 M_{\odot}$ and $17.6 M_{\odot}$. The mass ratio, initial period, and mass loss efficiency only marginally affect the predicted ranges.

Keywords: Binaries: close — Stars: evolution — Supernovae: general — Methods: numerical

1. INTRODUCTION

Two types of supernova explosions are thought to be responsible for the creation of neutron stars (NS) in the universe. While the majority of these explosions are the result of a collapsing iron core after fuel exhaustion (a so-called a core collapse supernova, CCSN, cf. [Woosley et al. 2002](#); [Heger et al. 2003](#); [Langer 2012](#)), a fraction of supernova progenitors most likely collapses as a result of the loss of pressure support due to electron captures on ^{24}Mg and ^{20}Ne ([Nomoto 1984](#)). These so-called electron capture supernovae (ECSN) are thought to occupy the lower end of the mass spectrum of supernova progenitors. ECSN thus form the transition between massive oxygen-neon (ONe) white dwarfs (WD) and supernovae. As the majority of massive stars are observed to be part of a binary system which could impact its evolution ([Kobulnicky & Fryer 2007](#); [Sana et al. 2012, 2013](#); [Duchêne & Kraus 2013](#); [Kobulnicky et al. 2014](#); [Almeida et al. 2017](#)), not only the observational properties of these stars will be very different from single stars, their final properties could also affect our understanding of the formation and evolution of NS+NS mergers which could be observed by the aLIGO/VIRGO network

([Abbott et al. 2016](#); [Côté et al. 2017](#)).

For single stars, the transition region between WD and CCSN, has been explored quite thoroughly. Pioneering work was done in the eighties by [Miyaji et al. \(1980\)](#); [Nomoto \(1984, 1987\)](#); [Miyaji & Nomoto \(1987\)](#), followed by further work in the late nineties ([Garcia-Berro & Iben 1994](#); [Ritossa et al. 1996](#); [Garcia-Berro et al. 1997](#); [Iben et al. 1997](#); [Ritossa et al. 1999](#)), and a final wave during the last ten years, some extending their models to lower metallicities ([Siess 2006, 2007, 2010](#); [Poelarends et al. 2008](#); [Takahashi et al. 2013](#); [Jones et al. 2013, 2014](#); [Doherty et al. 2010, 2014a,b, 2015](#)). The initial mass range, for which ECSN could occur in single stars, was initially predicted between $8 M_{\odot}$ and $10 M_{\odot}$, based on the mass of the helium core ([Nomoto 1984, 1987](#)). This was later refined, for solar metallicity stars, to a much narrower range, especially due to a better understanding of the effect of the second dredge-up which reduces the helium cores of stars in the relevant mass range down to below the Chandrasekhar mass ([Poelarends et al. 2008](#)). Uncertainties in mass loss rates during the final phase of the evolution of stars in this mass range, combined with a lack of general consensus regarding the treatment of

chemical mixing and convection in these stars, however, make that several estimates of the initial ECSN mass range now exist, ranging from $7 - 9 M_{\odot}$ (Woodsley & Heger 2015), $9 - 9.25 M_{\odot}$ (Poelarends et al. 2008) to $9.5 - 11 M_{\odot}$ (Siess 2006; Doherty et al. 2010; Takahashi et al. 2013). Fundamentally, however, the final fate of a star in this mass range is determined by a race between core growth and mass loss. If heating due to core growth is able to offset cooling due to neutrino losses the core will contract at a roughly constant temperature until a critical density is reached where electron captures can provide additional heating which will start O+Ne deflagration in the very center, leading to an explosion (Takahashi et al. 2013). However, if the star experiences a strong stellar wind at the end of its life (not unlikely for stars on the Asymptotic Giant Branch), it is possible that the entire envelop might be removed before the conditions necessary for electron captures are reached. In this scenario, the final fate would be a massive ONe WD (Poelarends et al. 2008).

The ECSN mass range, however, is expected to be different in close binary systems as the primary could potentially lose a significant fraction of its mass as a result of Roche lobe overflow (hereafter RLOF, cf. Wellstein et al. 2001; Langer 2012; de Mink et al. 2013). Podsiadlowski et al. (2004) speculated that ECSN could occur for primary masses between $8 M_{\odot}$ and $17 M_{\odot}$. They argued that systems that start mass transfer during core hydrogen burning (Case A) would give rise to much smaller helium cores, pushing the limit for ECSN toward higher initial masses. Systems that start mass transfer during or after hydrogen shell burning (Case B) would avoid the reduction of the helium core by the second dredge-up and could potentially form a bigger helium core, thus expanding the range also to lower initial masses.

Attention has recently turned to stripped-envelope stars in close binaries as possible progenitors of ECSN (Tauris et al. 2013, 2015; Moriya & Eldridge 2016). Motivated by recent discoveries of weak and fast optical transients, ECSN from close binaries have been suggested as a possible origin, due to the fact that through binary interactions, ECSN progenitors can lose most or all of their hydrogen envelope. Tauris et al. (2013, 2015) showed that a helium star companion to a neutron star may experience mass transfer and evolve into a ONe core with a mass of $\sim 1.5 M_{\odot}$ which in certain binary configurations may lead to an ECSN. Moriya & Eldridge (2016) explore the possibility of ECSN from mergers and the effects of common envelope evolution. They show that binaries with short orbital periods and fairly high mass ratios are able to experience a common envelope (CE) phase and a subsequent merger, after which the product of the merger is able to evolve into an ECSN with a small

amount of ejecta due to the significant mass loss during the CE phase and merger.

In this paper we explore the parameter space established by Podsiadlowski et al. (2004), primarily defined by primary masses between $8 M_{\odot}$ and $17 M_{\odot}$, to more accurately determine whether ECSN from close binary systems are indeed a possibility and which mass range they would occupy. The predictions of Podsiadlowski et al. (2004), however, were based on the helium core criterion as defined by Nomoto (1984, 1987). The validity of this criterion for binary systems, however, can be questioned as it is based upon the mass of the undisturbed helium core, and does not account for the effects of mass transfer. In addition, the mass range for single stars has been narrowed down a bit in subsequent studies, leading to the question whether the $8 - 17 M_{\odot}$ mass range for ECSN in close binaries, as estimated by Podsiadlowski et al. (2004), is still accurate. To investigate this, we created a large grid of models, covering most of the mass range suggested by Podsiadlowski et al. (2004).

In Section 2 we discuss our stellar evolution code, the input physics we employ, and the details of the grid. In Section 3 we present several representative systems and discuss the main impacts on the evolution of such systems. Section 4 investigates the role of mass loss due to Roche Lobe overflow, and the effects it has on the evolution of the core. In Section 5 we explore various pathways for ECSN in binaries, based on detailed models of the final evolution of the carbon core. In Section 7 we present updated values for the ECSN mass range in close binary systems. In Section 8 we consider the question how probable ECSN from close binaries are, and what the expected mass range for ECSN would be, and we compare our results with previous work on this topic.

Appendix A discusses the effects on our main results of different treatments of convective boundaries, and App. B discusses the robustness of our results through a resolution study.

2. METHODS AND GRIDS

2.1. *Stellar Evolution Code*

We used the MESA stellar evolution code (Paxton et al. 2011, 2013, 2015) (revision 8118) to model the evolution of a dense grid of binary stellar evolution models. Nuclear reactions were followed using the sufficiently detailed networks provided with MESA, i.e. `basic.net` for hydrogen and helium fusion, `co.burn.net` for carbon and oxygen fusion, and `approx21.net` for later phases. Opacities were calculated using tables from the OPAL project Grevesse & Noels (1993), with the initial metallicity set to $z = 0.02$ and metal fractions set according to Grevesse & Sauval (1998). Convection

was treated according to standard mixing-length theory (Böhm-Vitense 1958) with a mixing-length parameter $\alpha = 1.5$ using the Ledoux criterion to determine the location of convective boundaries. To maintain some degree of consistency with Wellstein et al. 2001, no additional mixing due to overshooting was incorporated in the models, and semi-convective mixing was modeled according to Langer et al. (1985) with $\alpha_{\text{sm}} = 0.01$. This choice, particularly to leave out any effects of overshooting, does have implications for the growth of the core and the removal of the envelope, and will potentially affect our final ECSN mass ranges. It has been well established (Maeder 1976; Siess 2007; Paxton et al. 2013) that using the Schwarzschild criterion for determining convective boundaries produces larger helium cores, especially when one includes a certain amount of overshooting. This will shift the ECSN mass range to lower initial primary masses. Overshooting also changes the response of the star to mass accretion and its ability to adjust its thermal structure, possibly leading to the secondary filling its Roche lobe at a different time, affecting the formation of contact in overshooting grids. We plan to perform a more comprehensive parameter study on the effects of convection criteria and overshooting in the future, but we have included a brief investigation into the effects of more efficient semi-convection, and the effects of overshooting in the context of the Schwarzschild criterion in Appendix A.

We modeled stellar winds according to the standard implementation in MESA (cool winds & hot winds), following Reimers (1975) for stars with surface temperatures below 10,000 K, and Kudritzki et al. (1987) for stars with surface temperatures above that. Mass transfer through Roche lobe overflow is calculated according to Ritter (1988) through the implicit scheme described in Paxton et al. (2015). MESA has the capability to handle accretion onto a critically rotating star, by either keeping the star at a set rotation rate (e.g. 98% of critical rotation) and rejecting additional accreted matter (cf. Paxton et al. 2015; Marchant et al. 2016) or by employing a scheme to enhance the mass loss at critical rotation (cf. Heger et al. 2000). However, as we aimed to test the sensitivity of our binary models to the mass transfer efficiency, we chose to set the mass transfer efficiency through Roche lobe overflow to fixed values. To avoid super-critical rotation of the secondary, we only follow the spin angular momentum of the primary; hence, we put the initial surface velocities at 100 km s^{-1} and 0 km s^{-1} for the donor and the accretor, respectively. We model the tidal interactions on the primary as described in Paxton et al. (2015) with the synchronization timescale for convective envelopes calculated according to Hurley et al. (2002). While there are varying definitions of the mass transfer efficiency

in the literature, in this study we use the definition $\beta = \dot{M}_{\text{lost}}/\dot{M}_{\text{RLOF}}$, the fraction of RLOF transferred mass that is lost from the system, i.e. the transferred mass that is not accreted onto the accretor (Tauris & van den Heuvel 2006). Mass leaves the system with the specific orbital angular momentum of the accreting star, while $(1 - \beta)$ is accepted by the accretor. In our grid we use β values of 0.0 (conservative, no mass lost from the system), 0.25, 0.50 and 0.75 (75% of the mass leaves the system).

2.2. Description of the Grid

To cover the full range of possible mass transfer scenarios in binaries, we calculated a dense grid of models with initial primary masses between $8.0 M_{\odot}$ and $14.5 M_{\odot}$ spaced by $0.25 M_{\odot}$, mass ratios ($q = M_2/M_1$) between 0.6 and 0.9 with a spacing of 0.1 and initial periods between 13 and 35 days with an interval of 1 day. A second, denser, grid was calculated with initial primary masses between 13.3 and $15.0 M_{\odot}$ with a spacing of $0.1 M_{\odot}$, mass ratios between 0.65 and 0.95 with a spacing of 0.05, and initial periods between 3 and 12 days with an interval of 1 day (0.5 days below 4.0).

Binary systems in in our grid generally undergo Case A or Case B mass transfer, with the primary losing a significant fraction of its mass before carbon burning commences. As we will discuss below, short period and long period systems (early Case A and Case B) and systems with extreme mass ratios are more prone to develop a contact system (cf. Wellstein et al. 2001). Once systems enter into contact, we don't follow their evolution further and ignore them in our analysis. Since presently MESA does not offer robust methods to compute common envelope evolution and/or mergers, it is unpractical to include these evolutionary paths in a parameter exploration study requiring large numbers of models. Therefore, we did not investigate models with initial periods below 3 days as in Moriya & Eldridge (2016). To avoid unnecessary computations in the late phases of the evolution we terminated the models at either neon ignition (which is for primaries in this mass range below $\log(\rho_c) = 8.25 \text{ g cm}^{-3}$, see Fig. 7) or $\log(\rho_c) > 8.5 \text{ g cm}^{-3}$, whichever comes first. To establish the final evolution of stars that did not ignite neon, we computed several models beyond $\log(\rho_c) > 8.5 \text{ g cm}^{-3}$ and results of these models will be discussed in Sec. 5.

2.3. Relevant Definitions for ECSN

We assume that stars with carbon-oxygen core masses (hereafter M_{CO}) below $1.37 M_{\odot}$ will not develop conditions conducive for electron captures on neon and magnesium (Jones et al. 2013; Takahashi et al. 2013), and that stars that develop neon burning (either central, or

for this mass range more likely, off-center) will end their lives as a CCSN (e.g. Jones et al. 2013; Woosley & Heger 2015). A recent study by Tauris et al. (2015) indeed found that helium stars in close binaries with M_{CO} in the $1.37\text{--}1.43 M_{\odot}$ mass range exploded as ECSN. While the threshold for neon burning in single stars is found at approximately $M_{\text{CO}} = 1.42 M_{\odot}$ (e.g. Jones et al. 2013; Woosley & Heger 2015), this is not necessarily the case for primaries in close binaries. As noted by Tauris et al. (2015), in addition to a core mass in a critical range, the core also needs to have a sufficiently high temperature for the onset of neon burning.

For stars that develop CO cores with M_{CO} above $1.37 M_{\odot}$ but do not ignite neon, we employ a method similar to the one first pioneered by Nomoto (1984) to determine the final fate based on the mass the core. However, since stars in our mass range undergo significant mass transfer through RLOF, which may affect the mass of the helium core (Wellstein & Langer 1999), we instead use the mass of the CO core instead of the helium core to determine the final fate of these stars. Throughout this paper we use the following definitions for the various core masses. A helium core boundary is defined at the outermost location where the hydrogen mass fraction is below 0.01 (i.e. a hydrogen free core). Similar definitions are used for the CO core (outermost mass location where the helium mass fraction is below 0.01), and the ONe core (outermost mass location where the carbon mass fraction is below 0.01).

In section 4 we analyze the conditions in stars that do not develop neon ignition. To determine whether conditions at a certain location are conducive for neon burning we calculated for a composition of 50% neon and 50% oxygen the neon burning energy generation and neutrino loss rate for densities and temperatures representative for our cores. The energy generation rate for neon burning was taken from Woosley et al. (2002) and the neutrino loss rate from Itoh et al. (1996), through Fortran routines provided by F.X. Timmes, available at http://cococubed.asu.edu/code_pages/nuloss.shtml. This allows us to infer, in terms of density and temperature, whether the conditions for dominant neon burning are met or not.

3. REPRESENTATIVE SYSTEMS: CASE A AND B

Before we discuss the details of our grid, we first consider a sample of representative binary evolution systems that illustrate the variety of outcomes that systems in this parameter range can experience. Every system is calculated with four different values of β from $\beta = 0$ to $\beta = 0.75$. As argued by Packet (1981), a little amount of matter can spin up the accretor to critical rotation, and it is assumed that the star can not accrete any more matter. However, it is still unclear how the star regu-

lates exactly how much it accretes (cf. Wellstein et al. 2001; de Mink et al. 2013), and there is evidence for both close-to-conservative systems (Langer et al. 2003) and for systems with close-to-non-conservative evolution (de Mink et al. 2007). Therefore, we take $\beta = 0.5$ as our reference case and discuss higher and lower mass transfer efficiencies for each case. This choice of β might be too high still, unless a disk is able to mediate the simultaneous accretion of matter and loss of angular momentum from the star through viscous stresses (cf. Paczyński 1991; Deschamps et al. 2013).

3.1. Case A Evolution

Systems where mass transfer starts during the core hydrogen burning phase of the donor are defined to be undergoing case A evolution. To start mass transfer during the core hydrogen burning stage of the primary star the system needs to have an orbital period below 3 days, although this is somewhat dependent on the initial mass and mass ratio (c.f. Wellstein et al. 2001). Many systems in our grid with Case A mass transfer lead to contact and could produce an ECSN through the merger scenario seen in Fig. 1a,b of Moriya & Eldridge (2016), or avoid evolution into an ECSN altogether. However, systems with periods of approximately 3–3.5 days, avoid contact and are able to produce a well developed CO core in the mass range for ECSN to occur.

We show the evolution of a representative system of this class on the Hertzsprung-Russell diagram in Fig. 1, its mass loss history in Fig. 2 and the evolution of its internal structure on the Kippenhahn diagram in Fig. 3. This particular system has an initial primary mass of $15.7 M_{\odot}$, a secondary mass of $12.56 M_{\odot}$ (corresponding to $q = 0.8$), an initial orbital period of 3 days and is evolved with $\beta = 0.5$. The primary reaches its Roche lobe after 0.94×10^7 years (see Fig 1, 3) when the helium mass fraction in the core is 0.89. This initiates mass transfer through RLOF. As seen in Fig. 2, this initially takes place at a fairly high rate (thermal time scale) as the donor adjusts to the decreasing orbital separation. This is the so-called rapid Case A mass transfer phase (Pols 1994; Wellstein et al. 2001), during which the primary loses about $9 M_{\odot}$. After the mass ratio reverses, the mass transfer slows down to values around $\sim 10^{-6} M_{\odot} \text{ yr}^{-1}$, driven by the nuclear evolution of the star.

During this phase the star loses another $0.4 M_{\odot}$, and finishes this first mass transfer phase with a total mass of $6.23 M_{\odot}$, and a helium core mass of $1.75 M_{\odot}$. The ignition of the hydrogen burning shell causes the star to expand, attempting to grow to red giant dimensions, which starts the second mass transfer phase, the so-called Case AB phase (i.e. a case B mass transfer phase following a case A, Wellstein et al. 2001), which proceeds on the

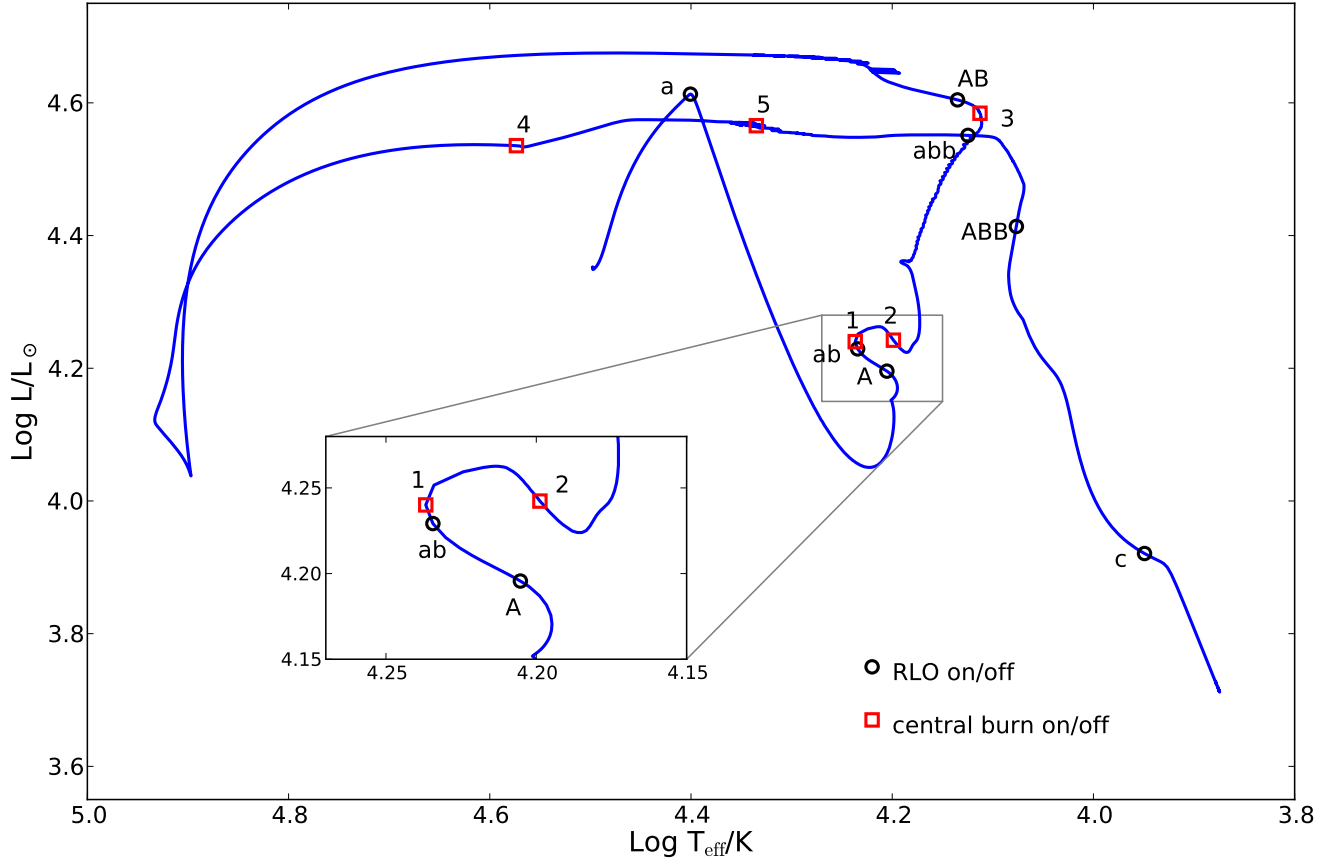


Figure 1. HR diagram of the evolution of the primary star in a system with a primary mass of $15.7 M_{\odot}$, a secondary mass of $12.56 M_{\odot}$ ($q = 0.8$), an initial orbital period of 3 days and a β parameter of 0.5. The start and end of RLOF is indicated with a black circle: case A (on:a, off:A), case AB (on:ab, off: AB), case ABB (on:abb, off:ABB), case C (on:c). The start and end of central nuclear burning is indicated with a red square: central hydrogen burning off (1), central helium burning on (2), off (3) and central carbon burning on (4) and off (5).

thermal timescale of the star. During this phase mass transfer rates are of the order of $3 \times 10^{-5} M_{\odot} \text{ yr}^{-1}$, and the star loses an additional $3 M_{\odot}$ so that the total mass left is $3.24 M_{\odot}$ (which, in this system, corresponds to the mass of the convective hydrogen core at the time Case A mass transfer started, see Fig. 3). At this time the helium core measures $2.13 M_{\odot}$, which through subsequent hydrogen shell burning grows to $3.08 M_{\odot}$. Once Case AB mass transfer finishes, the star is able to adjust its structure and thereby its radius to recover hydrostatic equilibrium. As a result, the radius of the star decreases, the temperature increases, and the star moves to the left side of the Hertzsprung Russell diagram, becoming a hot and compact helium star (see Fig 1). The star finishes helium core burning at 1.172×10^7 yr and subsequent core compression ignites helium shell burning, which expands the star again to red giant dimension, starting another mass transfer episode (Case ABB). By the time that convective carbon burning starts in the core, a CO core of $1.29 M_{\odot}$ has formed. Throughout the carbon burning phase (various carbon flashes), which

lasts from 1.192×10^7 yr till 1.194×10^7 yr (about 20,000 yrs), the star forms a core composed of neon and oxygen. Another episode of mass transfer starts during the final carbon flashes (the third panel in Fig. 2, also marked in Fig. 3) which erodes the final bit of the remaining hydrogen layer and cancels hydrogen burning.

By the end of carbon burning the ONe core has a mass of $1.19 M_{\odot}$ while the CO core has a mass of $1.34 M_{\odot}$. During the last carbon shell flash a convective shell forms on top of the helium burning shell, which slowly diminishes the helium burning intensity. This also slows down the growth of the CO core, which is able to grow to a mass of $1.40 M_{\odot}$ by the end of the model run. Significant mass loss develops at the very end of the model run and causes instabilities that terminate the model (see also Section 5). During the evolution of the primary, the secondary has grown by $\sim 6 M_{\odot}$ to a total mass of $18.58 M_{\odot}$. Although it is now much more massive than the primary, it is still a main sequence star (hydrogen mass fraction of 0.03) due to the accretion of large amounts of fresh hydrogen, causing the star to re-

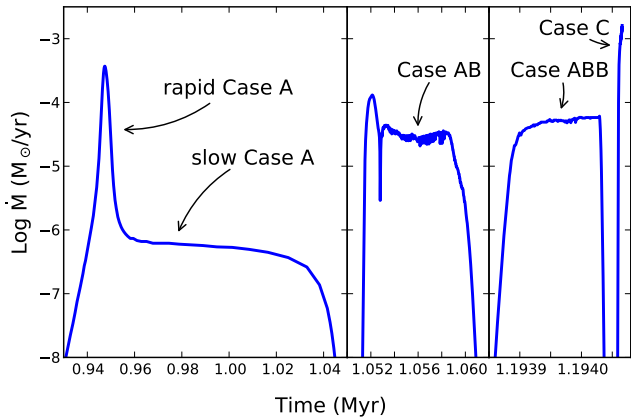


Figure 2. Details of the mass transfer rate as a function of time for Case A system. Three distinct phases are visible. The left panel shows the mass transfer rate during core hydrogen burning. The middle panel shows the mass transfer rates during hydrogen shell burning. The last panel shows mass transfer rates during and after carbon burning, cf. Fig. 3. The rise in mass transfer rate at the very end is a result of instabilities arising in the envelope and will be discussed in Sec. 5.

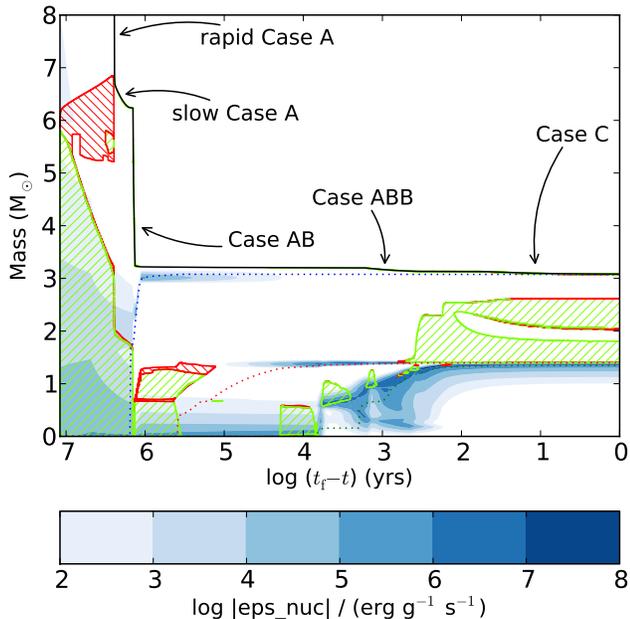


Figure 3. Kippenhahn plot of the donor of our Case A system. The total mass is indicated by the solid black line. The green hatched regions indicate areas of convection, while the red hatched regions indicate semi-convection. Regions of nuclear energy generation are marked with blue shading. Only the inner $8 M_{\odot}$ of the initially $15 M_{\odot}$ star are shown. As the later phases in the evolution take place on a much shorter timescale, the x-axis is plotted with a logarithmic scale.

juvenate (Hellings 1983; de Mink et al. 2014; Schneider et al. 2016). If the primary is able to explode and form a neutron star, this system most likely evolves into an Be/X-ray binary.

Systems with a different mass transfer efficiency display a similar behavior, although the orbit widens more rapidly for less conservative mass transfer, and less rapidly for more conservative mass transfer. This results in slightly larger final M_{CO} for stars with $\beta = 0.75$ and slightly smaller final M_{CO} for stars with $\beta = 0.0$ and 0.25 , compared with our fiducial case of $\beta = 0.5$. Due to the different rates at which the orbit responds to mass transfer and loss for various values of β , the number and the intensity of RLOF episodes also shows some variation, but since mass transfer is primarily driven by changes in the thermal structure of the primary, in the end, similar final outcomes are found.

3.2. Case B Evolution

Stars that undergo their first mass transfer phase during hydrogen shell burning are considered Case B mass transfer systems. The removal of high-entropy layers of the envelope causes the star to shrink on a dynamical timescale, however, as the donor expands on the thermal timescale during the crossing of the Hertzsprung gap this leads to stable but high mass transfer rates of $\sim 10^{-4} - 10^{-3} M_{\odot} \text{ yr}^{-1}$, with a distinguishable fast and subsequent slower rate as the orbit initially shrinks and then widens again (c.f., Fig 4). Differences in the timing of the start of mass transfer, due to different initial periods, lead to significant different evolutionary paths. Early Case B mass transfer will appreciably affect the formation of the helium core as the intensity of hydrogen shell burning is diminished as a result of the envelope responding to the high mass loss rates. Late Case B mass transfer will have less of an effect as the helium core has already been established by the time mass transfer starts. Variations in the value of β also cause notable differences. Systems that evolve conservatively or nearly conservatively, have a higher chance to develop contact, because of two associated effects. As less mass is lost from the system, the accretor gains mass faster, and hence fills its Roche lobe earlier, leading to more contact systems. This effect is stronger for systems with $q \ll 1$ as the initial Roche lobe of the accretor is much smaller than for systems with a mass ratio close to 1. However, in addition, initially wider systems, develop higher mass loss rates as they are further into the Hertzsprung gap (c.f. Wellstein et al. 2001; Pols 1994) which pushes the accretor further out of equilibrium. As the accretor is still a main sequence star and has a radiative envelope, mass accretion makes it swell considerably, leading to contact. On the other hand, systems that evolve more non-conservatively than our fiducial model show more con-

tact free evolution up to higher initial periods, because the accretor does not gain as much mass and accretes it at lower rates as most of the mass is leaving the system, making it less prone to swell up and reach its Roche lobe. Because the time of the beginning of Case B mass transfer has a strong influence on the subsequent evolution, we discuss three different Case B systems in order to establish a clear picture of Case B evolution.

Fig. 4 shows the evolution of three Case B systems (an early, mid, and late Case B system). System 1 (top row), an early Case B system ($M_1 = 14.0 M_\odot$, $M_2 = 11.2 M_\odot$, $P_{\text{init}} = 4$ days), started mass transfer promptly after the primary star finished core hydrogen burning and started crossing the Hertzsprung gap ($t_{\text{RLOF1}} = 11.6998$ Myr). Mass transfer rates of $\sim 10^{-3} M_\odot \text{ yr}^{-1}$ are seen for approximately 10,000 yrs during which the orbit shrinks and the primary loses $9.8 M_\odot$. After the mass ratio reverses and the orbit widens again as a response to the mass transfer, the star is able to adjust its thermal structure, and around 11.71 Myr a period of slower mass transfer commences (slow Case B, Paczyński 1971; Doom 1984) with rates of $\sim 3 \times 10^{-5} M_\odot \text{ yr}^{-1}$ (Fig 4, top right). The separation of the binary components increases from $31 R_\odot$ at the start of Roche lobe overflow to $\sim 100 R_\odot$ after the fast Case B phase, and $150 R_\odot$ (48 days) after the first mass transfer phase finishes (i.e. when helium ignited in the core). During hydrogen shell burning, the core of the star continues to contract until helium ignites in its core. This allows the star to readjust its thermal structure again, and the star shrinks in response to this, detaches from its Roche lobe, and experiences a pause in mass transfer. As a result, the star is able to evolve through core helium burning relatively unaffected. After helium core burning the primary has a mass of $3.3 M_\odot$, with a helium core of $3.11 M_\odot$ and a CO core of $1.29 M_\odot$. Continued contraction heats up the core and layers above, until the helium shell ignites. The envelope readjusted its thermal structure once again through expansion, fills its Roche lobe and restarts mass transfer through Roche lobe overflow during the subsequent core carbon burning phase (case BB, $t_{\text{RLOF2}} = 13.0534$ Myr). This phase only lasts for $\sim 20,000$ years at a rate of $\sim 5 \times 10^{-5} M_\odot \text{ yr}^{-1}$ during which the star loses its residual hydrogen layer of $0.2 M_\odot$. A final mass loss episode starts at $t_{\text{RLOF3}} = 13.0688$ Myr (Case BBC), which after ~ 100 years leads to instabilities that terminate the model. At the end of its evolution the star has established an helium core of $3.12 M_\odot$, a CO core of $1.40 M_\odot$ and an ONe core of $1.35 M_\odot$. The final orbital separation of the system is $\sim 175 R_\odot$.

The same system, evolved with different values of β gives fairly similar evolutionary outcomes, although with slightly less massive CO cores for more conservative evolution and slightly more massive CO cores for

less conservative evolution. All systems avoid contact, due to their small initial orbital period, but the systems with more conservative mass transfer develop smaller CO cores as a result of a tighter system and hence prolonged mass transfer.

System 2 (Fig. 4, middle row) is a binary system ($M_1 = 14.0 M_\odot$, $M_2 = 11.2 M_\odot$, $P_{\text{init}} = 15$ days) that experiences the start of Roche lobe overflow in the middle of the Hertzsprung gap ($t_{\text{RLOF1}} = 11.7210$ Myr). As a result of the natural expansion of the star and the shrinking orbit, mass transfer rates quickly increase to values of $\sim 5 \times 10^{-3} M_\odot \text{ yr}^{-1}$ during which $10.4 M_\odot$ is lost from the primary, leaving a donor with a mass of $3.6 M_\odot$, a helium core of $3.18 M_\odot$ and a CO core of $1.31 M_\odot$ at the completion of core helium burning. Due to adjustments to the thermal structure of the star during the contraction of the CO core, mass loss increases again during the carbon burning phase (Fig. 5, middle row, Case BB, $t_{\text{RLOF2}} = 13.0237$ Myr), but now at relatively low rates of $\sim 7 \times 10^{-5} M_\odot \text{ yr}^{-1}$. This moderate mass loss removed almost the entire residual hydrogen envelope, and leaves a star with mass of $3.23 M_\odot$, a He core of $3.22 M_\odot$, a CO core of $1.42 M_\odot$ and a ONe core of $1.38 M_\odot$. A third, case BBC, mass transfer phase, starts at $t_{\text{RLOF3}} = 13.0345$ Myr, but only removes $0.01 M_\odot$ before it terminates due to instabilities that develop in the envelope. During the fast Case B mass transfer period, the orbit increased from $75 R_\odot$ (initial) to $345 R_\odot$, which increases during subsequent mass loss episodes to $370 R_\odot$. While the initial period of this system was quite a lot larger than system 1, the evolution of system 2 proceeded very similar to that of system 1. While system 1 starts mass transfer earlier, system 2 reaches higher mass transfer rates due to its higher mass and shorter Kelvin-Helmholz timescale. Both mass loss episodes terminate when helium ignites in the core (roughly about the same time, $t = 1.1742 \times 10^7$ yr, see Fig. 4), and consequently the amount of mass transferred during the first mass transfer phase is about equal ($\sim 10 M_\odot$).

Evolving this system with different values of β shows that the most conservative scenarios ($\beta = 0, 0.25$) lead to contact during RLOF, while the systems with $\beta = 0.5, 0.75$ are able to avoid contact. This is the result of a faster growing, and thus quicker swelling accretor in the case of conservative mass transfer, while systems with largely non-conservative evolution don't accrete as much matter onto the secondary, avoiding an expansion of their radius beyond their Roche lobe and hence contact all together.

System 3 (Fig. 4, bottom row) shows the evolution of a binary system ($M_1 = 14.0 M_\odot$, $M_2 = 11.2 M_\odot$, $P_{\text{init}} = 25$ days) that experiences the start of Roche lobe overflow late in the Hertzsprung gap ($t_{\text{RLOF1}} = 11.7250$ Myr). As the primary expands beyond its Roche

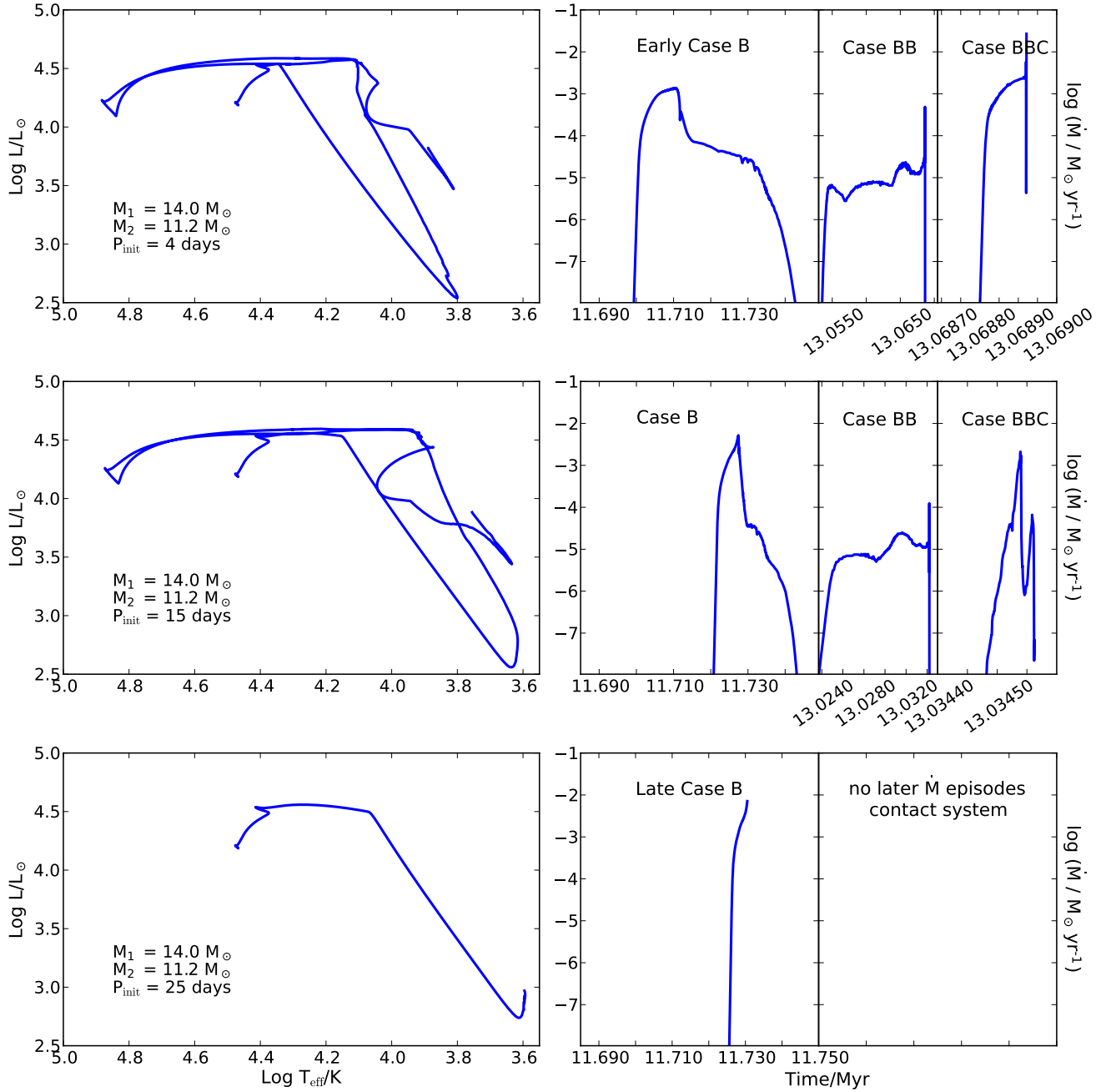


Figure 4. Evolution of a binary system with $M_1 = 14.0 M_\odot$ and $M_2 = 11.2 M_\odot$, with three different initial orbital periods, corresponding to early Case B mass transfer (4 days, top row), intermediate Case B mass transfer (15 days, middle panel) and late Case B mass transfer (25 days, bottom panel). The left column shows the Hertzsprung-Russell diagram for the three systems, the right column shows the mass transfer history as a function of time for the three systems. While the first window of each mass loss panel has the same scale and allows for comparison between the timing of the onset of mass transfer, later phases are zoomed in considerably to show detail and have different scales on the time axis.

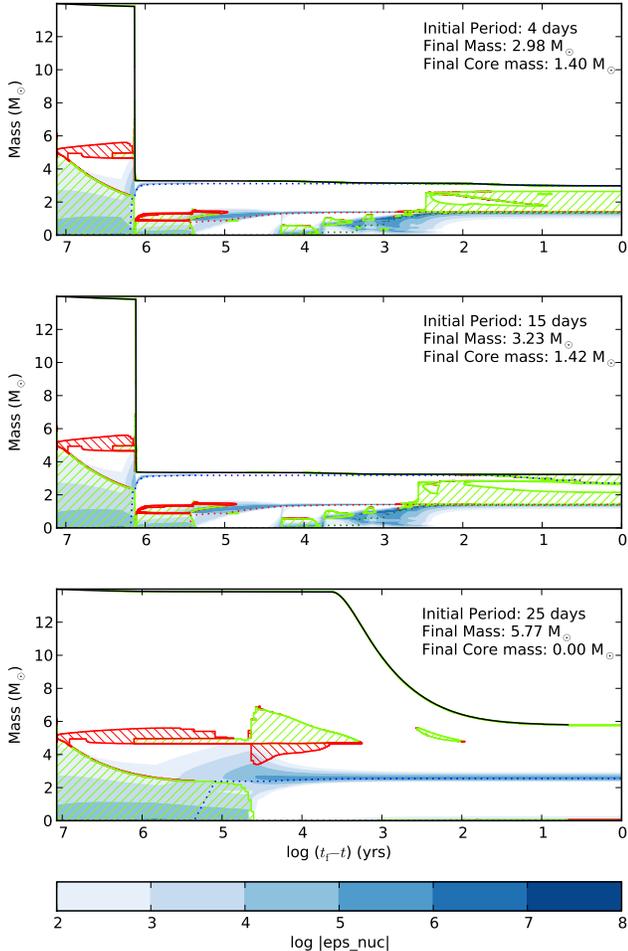


Figure 5. Kippenhahn diagrams for three Case B systems discussed in the text. The total mass is indicated by the solid black line. The green hatched regions indicate areas of convection, while the red hatched regions indicate semi-convection. Regions of nuclear energy generation are marked with blue shading. Time is plotted on the x -axis, with the value of $t_f - t$ /yr indicating the remaining time in the calculation, plotted logarithmically to show detail in the later phases of the evolution.

lobe, mass transfer rates quickly ramp up to values of $7.7 \times 10^{-3} M_{\odot} \text{yr}^{-1}$. Although the orbital separation increases, and thus the size of both Roche lobes, the secondary quickly fills its Roche lobe due to the large amount of accreted matter, leading to a contact system after only 4500 yrs (cf. de Mink et al. 2008b; Langer 2012; de Mink et al. 2013).

When evolved with different values of β , only the $\beta = 0.75$ is able to avoid contact, as the lower mass accretion rates and faster growing orbit allow the accretor to respond more efficiently to mass accretion, leading to less swelling and avoiding contact.

4. THE EFFECTS OF MASS LOSS ON THE EVOLUTION OF THE PRIMARY

In order to explode as an ECSN several ingredients need to be in place. Nomoto (1984) argued that stars with helium cores between 2.0 and $2.5 M_{\odot}$ (which corresponds to roughly to initial masses between 8 and $10 M_{\odot}$) would explode as an ECSN. His models, however, did not develop a second dredge-up which can significantly reduce the mass of the helium core and diminishes the predictive power of this criterion (cf. Podsiadlowski et al. 2004; Poelarends et al. 2008). Since then, several authors (Siess 2007; Poelarends et al. 2008; Jones et al. 2013; Doherty et al. 2010, 2015) have established precise initial mass ranges for ECSN to occur, although these mass ranges are highly sensitive to the adopted convection criteria, overshooting and mass loss prescriptions (Poelarends et al. 2008; Doherty et al. 2010; Langer 2012). Jones et al. (2013) produced several detailed models, computed all the way to electron captures on ^{24}Mg and ^{20}Ne , and found that CO cores with masses over $1.35 M_{\odot}$ are able to reach densities high enough for this to occur ($\log \rho \approx 9.6 \text{ g cm}^{-3}$). If the CO core is massive enough, neon will ignite off center (Jones et al. 2013; Schwab et al. 2016), but Jones et al. (2014) also found that the upper boundary for ECSN is affected by uncertainties regarding the progression or stalling of the neon flame. There seems to be consensus, however, that the mass of the CO core is a reliable indicator for the final fate of stars in this mass range. How this translates into the initial mass of the star, depends on the adopted convection criterion, with the Schwarzschild criterion producing more massive cores than the Ledoux criterion for the same initial mass. Inclusion of overshooting will also lead to larger cores (cf. Siess 2007). However, although the initial mass range for ECSN is therefore quite sensitive to the adopted convection criteria, this does not seem to be the case for the final M_{CO} as most authors find similar values for M_{CO} at which neon ignites, even though they treat convection differently. In the context of binary evolution, this provides an additional reason to adopt M_{CO} as indicator for whether the star explodes as an ECSN or not, as the CO core is generally not eroded by mass transfer, in contrast to the He core.

The question, however, is whether the range in M_{CO} for ECSN in binaries is identical to the established M_{CO} range for ECSN in single stars. Our models indicate that this might not necessarily be the case. Whereas CO cores with a mass of $\sim 1.42 M_{\odot}$ in single stars would ignite neon in their cores (cf. Nomoto 1984, 1987; Jones et al. 2013) our models do not show neon ignition due to a slightly lower central temperature. This rather different behavior is a direct result of the binary interaction, and thus unique to binary systems. We have identified, and will describe below, two processes that are responsible for that. Compared to single stars, significant mass loss before the establishment of the CO core will create

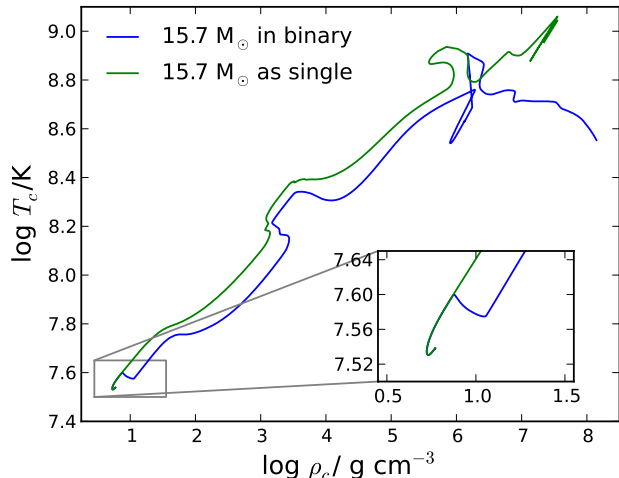


Figure 6. Evolution of the central density versus central temperature. Shown in blue is our Case A model which undergoes mass transfer once the core temperature reaches $\log T_c/K = 7.6$. Shown in green is a single star model of the same initial mass ($15.7 M_\odot$). As shown in the inset, the star that undergoes mass transfer develops a core that is cooler and more compact (higher density) compared to a single star of the same initial mass. The single star eventually develops off center neon burning and a CO core with a mass of $1.63 M_\odot$, while the star in the binary avoids neon burning and develops a CO core of $1.40 M_\odot$.

a smaller CO core and lead to a consistently lower temperature for the rest of its life. In addition, mass loss during and after carbon burning will cause the primary star to cool down faster compared to its single star counterpart even if the core mass is the same.

4.1. Mass Loss During Hydrogen or Helium Burning

Significant mass transfer due to RLOF anytime before the establishment of the CO core will affect the subsequent formation of the CO core. In Fig. 6 we show the evolution of the core in the ρ_c - T_c plane for the Case A system which we discussed in Sec. 3.1. The evolution for a single star, which is not affected by mass transfer, is shown as a comparison. As a response to the high mass loss rates and to compensate for the loss of $9 M_\odot$ of matter during the fast Case A phase, the core of the primary tries to restore hydrostatic equilibrium by contracting to higher densities. This results in a convective core which is $1 M_\odot$ smaller than an undisturbed core (see Fig. 3). A new equilibrium is found at a central temperature which is 2.6 million Kelvin lower than the central temperature before mass loss. As a result, stars that undergo Case A mass transfer form smaller convective cores than their single star counterparts, which results in the formation of smaller CO cores after He burning.

Case B systems do not show the notable decrease in central temperature upon the start of mass transfer, as

the hydrogen burning shell acts as a barrier between the exterior and the interior. As the core is contracting and heating up to allow for the start of He burning, the hydrogen shell is supporting the entire envelope independently of the core. However, as the envelope is quickly being reduced in mass, the outward progression of the hydrogen shell is limited by whatever is left over of the envelope, and hence not able to proceed as far outward as in cores not affected by RLOF (cf. Fig. 5).

The net effect of mass transfer before the establishment of the CO core is that the resulting CO cores are smaller and cooler than those of single stars.

4.2. Mass Loss After Core Carbon Burning

After central carbon burning, in the absence of a heat source, the core contracts again to maintain hydrostatic equilibrium. Due to this contraction at high central densities, thermal neutrino losses increase and degeneracy sets in, resulting in a degenerate core which is governed by the balance between heating due to contraction and cooling due to neutrino losses (Paczynski 1971; Nomoto 1984; Brooks et al. 2016). In single stars, hydrogen and helium shell burning would cause the core to grow, and cooling as a result of neutrino losses would be offset by additional heating as a result of accretion due to core growth. Even though a strong stellar wind, driven by helium shell flashes, can develop in the final phases of the lives of single stars, the center of these stars is able to maintain a more or less constant temperature, while contracting to densities conducive for electron captures to start. However, all of our models experience significant mass transfer due to RLOF during the carbon shell flash phase (with rates up to, and sometimes exceeding, $\dot{M} > 10^{-3} M_\odot \text{yr}^{-1}$). This pushes the star out of thermal equilibrium, leading to additional cooling in the core as a result of an endothermic expansion to make up for lost envelope matter (an effect similar to what has been found by Tauris et al. 2015; Schwab et al. 2016).

Fig. 7 shows the effect of high mass loss rates this late in the evolution of the star on the central temperature. The top row shows the central and conditions at T_{max} for a single star –not affected by mass transfer– with mass of $12.48 M_\odot$, which has developed a CO core with a mass of $1.33 M_\odot$. After central carbon burning, the ONe core contracts to higher densities. Due to the weak temperature dependence of the electron degenerate pressure and the strong sensitivity of the plasma-neutrino emission rate to the temperature and density, a temperature inversion will develop in the ONe core (Nomoto 1984). Because of high density, the center of the star experiences strong neutrino cooling, while the layers further outward experience less cooling or even some heating due to their proximity to the carbon and helium shell sources. Eventually the location of T_{max} can

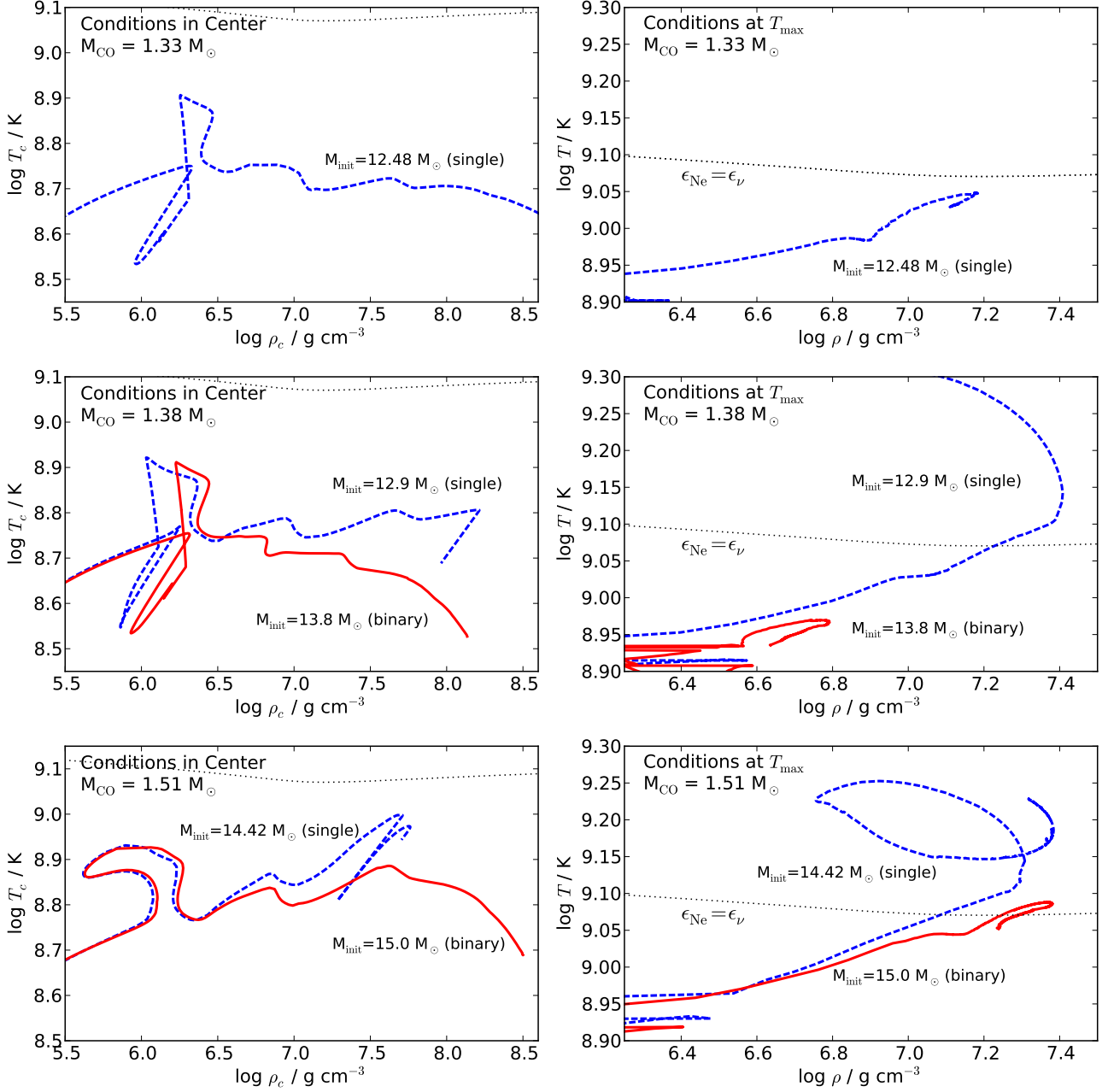


Figure 7. Evolution of the central density vs central temperature (left column) and density and temperature at the location of the maximum temperature (right column) for various single and binary models. The dotted line around $\log T / \text{K} = 9.1$ indicates conditions where neon burning and neutrino losses are in balance. The top row shows the evolution of a single star with an initial mass of $12.48 M_{\odot}$. The middle row shows the evolution of a single star with an initial mass of $12.9 M_{\odot}$ and a binary component with an initial mass of $13.8 M_{\odot}$. Both develop a CO core with a mass of $1.38 M_{\odot}$, with the single star evolving through neon burning and the binary component avoiding neon burning. The bottom row shows the evolution of a single star with an initial mass of $14.42 M_{\odot}$ and a binary component with an initial mass of $15.0 M_{\odot}$. Both develop an CO core with a mass of $1.51 M_{\odot}$, with the binary component narrowly avoiding sustained neon burning.

be found somewhere between the center and the carbon burning shell (cf. Figs. C1, C2 in Schwab et al. 2016). The conditions in the center are shown in the top left panel, while the conditions at T_{\max} are shown in the top right panel. In single stars, where mass loss is due to stellar winds instead of RLOF, we find a steady increase of the maximum temperature as a result of core growth due to helium and carbon burning. In this case, the CO core is not massive enough to reach neon ignition, and as can be seen in the top right panel, the temperature reaches a maximum and then decreases again, showing a characteristic hook. This hook can be understood as the whole core now succumbing to intense cooling as a result of thermal neutrino losses, and the mass coordinate of T_{\max} moving outward to lower densities, eventually merging with the carbon burning shell. If the core, however, is more massive (see middle and bottom panel of Fig. 7), the conditions at T_{\max} become conducive for neon ignition (shown by the blue dashed line crossing the $\epsilon_{\text{Ne}} = \epsilon_{\nu}$ line), causing the core to expand (shown by the hook in the blue dashed line in the left middle and left bottom panels). In the case of a CO core with a mass of $1.38 M_{\odot}$ ignition takes place at a radial mass coordinate of $0.95 M_{\odot}$, with ignition closer to the center for higher M_{CO} (Schwab et al. 2016).

When we compare, however, the evolution of the primary star in a binary (affected by significant past and ongoing mass loss) with the evolution of a single star as described above, we find some remarkable differences. The red lines in the middle and bottom row of Fig. 7 are for a binary component with the same M_{CO} as the single star shown in these panels. As can be seen in the middle left panel ($M_{\text{CO}} = 1.38 M_{\odot}$ for both models), carbon burning in the binary component ($M_{\text{init}} = 13.8 M_{\odot}$, $P_{\text{init}} = 9$ days) takes place at a slightly higher density than in the single star, a consequence of the compact core that has developed as a result of prior Case B RLOF. During the contraction phase after core carbon burning, however, the core cools down whereas the core of the single star heats up. The evolution of T_{\max} is also different, with the single star rapidly evolving toward conditions conducive for neon ignition, but the binary component reaching a maximum temperature of $\log(T/\text{K}) = 8.97$, by far not sufficient for neon ignition. The situation is similar for the binary model in the lower panel ($M_{\text{init}} = 15.0 M_{\odot}$, $P_{\text{init}} = 9$ days), which develops a CO core with a mass of $M_{\text{CO}} = 1.51 M_{\odot}$. This is far above the accepted M_{CO} for neon ignition in single stars, but our model fails to produce sustained neon burning, even though it briefly develops conditions conducive for neon ignition.

This difference in minimum M_{CO} needed for neon ignition between single stars and binary stars is also seen in Fig. 8 (left panel) where we plot the final M_{CO} against

the maximum temperature that a core attained during its evolution. The horizontal dotted line shows the approximate temperature that is necessary for neon to ignite, and forms the boundary between CCSN and ECSN. For simplicity we take a value of $\log T/\text{K} = 9.1$, although this might vary slightly depending on the density as the right panel shows. The red crosses represent single star models with initial masses from $12.0 - 13.0 M_{\odot}$ (spaced by $0.05 M_{\odot}$). These cross the $\epsilon_{\text{Ne}} = \epsilon_{\nu}$ line at $M_{\text{CO}} = 1.37 M_{\odot}$, in good agreement with Nomoto (1984); Jones et al. (2013); Takahashi et al. (2013); Schwab et al. (2016). The filled symbols represent several binary model runs. Binary Sequence A consists of stars with initial parameters: $M_1 = 13.8 - 15.2 M_{\odot}$ (spaced by $0.1 M_{\odot}$), $q = M_2/M_1 = 0.8$, and $P_{\text{init}} = 15$ days. Binary Sequence B consists of stars with initial parameters: $M_1 = 13.5 - 15.5 M_{\odot}$ (spaced by $0.1 M_{\odot}$), $q = M_2/M_1 = 0.9$, and $P_{\text{init}} = 20$ days. Binary Sequence C consists of stars with initial parameters: $M_1 = 13.6 - 15.2 M_{\odot}$ (spaced by $0.1 M_{\odot}$), $q = M_2/M_1 = 0.8$, and $P_{\text{init}} = 9$ days. All sequences have a mass transfer efficiency of $\beta = 0.5$. They all converge on one line, and as can be seen in the left panel of Fig. 8, the slope of this line is lower, and the maximum mass for neon ignition is shifted to considerably higher M_{CO} compared to the single star models. This line only crosses the $\epsilon_{\text{Ne}} = \epsilon_{\nu}$ line at $M_{\text{CO}} = 1.52 M_{\odot}$. The conclusion is that stars in binaries, experiencing high RLOF mass transfer rates, need $M_{\text{CO}} > 1.52 M_{\odot}$ to be able to develop conditions that will lead to neon ignition. In the right panel of Fig. 8 we plot the maximum temperature attained by the binary sequences and the single star sequence on a $T-\rho$ diagram. The fact that all sequences converge onto one line is compelling evidence that the CO cores in binaries behave physically the same, but undergo much stronger cooling than their single star counterparts, resulting in higher M_{CO} needed to ignite neon. Alternatively one could argue that these cores have, as a result of RLOF contracted to such high densities already, that further contraction is not able to raise the temperature in their cores to levels that could start neon ignition. To this effect, the neon ignition boundary shown in Fig. 12 and Fig. 13 is positioned at a $M_{\text{CO}} = 1.52 M_{\odot}$, which we take as the boundary between possible ECSN progenitors (lower masses) and CCSN progenitors (higher masses). See Appendix A for evidence that this shift in critical M_{CO} for neon ignition is independent of the adopted treatment of convective boundaries or the inclusion of overshooting.

5. THE EVOLUTION OF THE COOLING CORE TOWARDS ECSN

As argued by Takahashi et al. (2013), core contraction leading up to an ECSN goes through four dis-

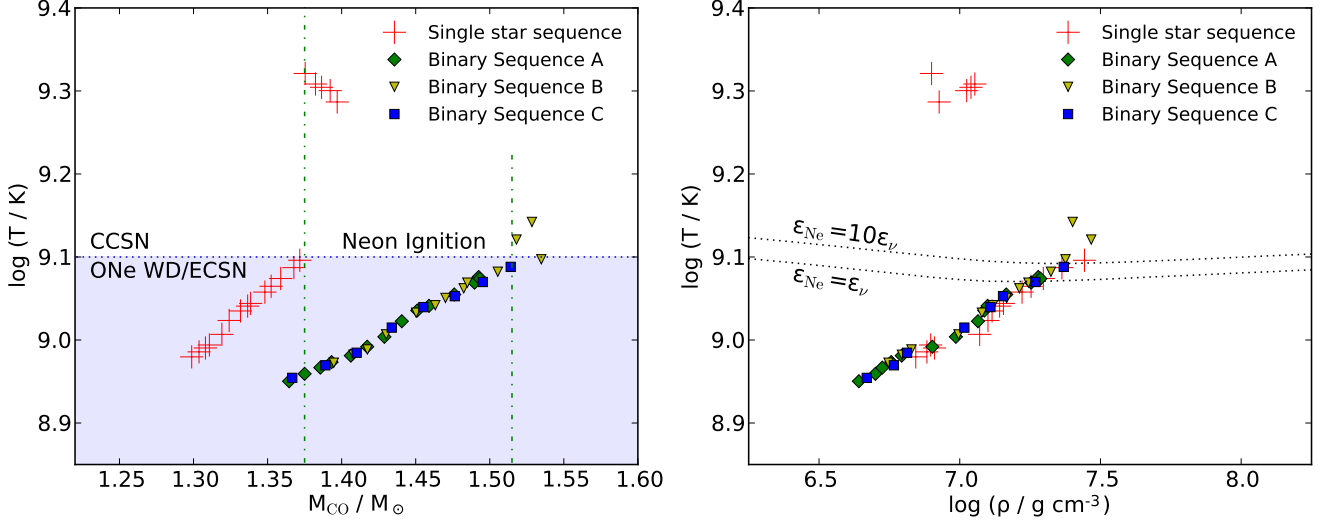


Figure 8. Maximum temperature attained in the core as a function of M_{CO} (left panel) and as a function of the density at the mass coordinate of T_{max} at the time of T_{max} (right panel), for single stars (red crosses) and primary stars in a binary system (filled symbols). The dotted line in the left panel approximates the critical temperature for neon ignition, while the dotted lines in the right panel give the locations where the energy generation of neon burning is equal to, and 10 times exceeds the energy losses due to thermal neutrinos.

tinct phases: First, neutrino cooling; second, core mass growth; third, electron captures on ^{24}Mg and ^{20}Ne and finally $\text{O}+\text{Ne}$ deflagration. As our models show much stronger cooling than single star models, the question is how this will affect the subsequent evolution toward electron captures. Based on our models we see three possible scenarios, which all could be realized in various systems, depending on the initial conditions.

The first possibility is based on scenario proposed by Paczyński (1971) and further developed by Schwab et al. (2015); Brooks et al. (2016). In this scenario, the ONe core continues to increase in density and electrons become increasingly degenerate. As a result, the evolution of the core is more and more dominated by the balance between compressional heating and neutrino cooling. Compressional heating is a result of the gravitational contraction and core growth due to helium and carbon shell burning, while neutrino cooling is primarily due to thermal neutrino emission. As the density increases and the core temperature decreases, cooling due to plasma-neutrinos becomes less efficient, and eventually compressional heating slows down the cooling of the core. At some point in time, the neutrino cooling timescale, $\tau_{\nu} = c_p T / \epsilon_{\nu}$, equals the compression timescale, $\tau_{\text{comp}} = (d \ln \rho / dt)^{-1}$, and the evolution of the core will proceed along a trajectory which is primarily dependent on the core growth rate (Paczynski 1971; Brooks et al. 2016). When high enough densities are reached, URCA processes will accelerate the contraction of the core toward densities where electron captures on ^{20}Ne and ^{24}Mg will induce core collapse.

The second possible evolutionary scenario is prompted by some indications in our models that the primary enters a final mass transfer episode. Many of our models developed significant envelope instabilities during the final stages of their evolution (case ABC or BBC), which drove mass transfer rates up considerably. It is possible that this final episode of mass transfer removes the entire envelope, after which the remnant shrinks and mass transfer ceases, leaving a massive ONe core with possibly a thin CO shell around it. As this core is not able to grow anymore it will cool down and leave a massive, super-Chandrasekhar ONe WD. Evidence for super-Chandrasekhar white dwarfs comes from several peculiar Type Ia supernovae, e.g. SN 2006gz, SN 2007if, SN 2009dc (Hicken et al. 2007; Scalzo et al. 2010; Taubenberger et al. 2011) and theoretical considerations into their existence (e.g., Das & Mukhopadhyay 2013; Subramanian & Mukhopadhyay 2015, for an arguments against their existence, see Manreza Paret et al. 2015). To account for these super-Chandrasekhar cores, however, a strong magnetic field is required, and as we did not take magnetic fields into account in our models, we are not able to verify the existence of magnetic fields in these massive ONe cores.

The third possible scenario also takes its cues from the final mass transfer episode, but suggests that the intensity of the mass transfer will lead to the secondary filling its Roche lobe, leading to common envelope evolution. If this scenario develops, the binary components will enter a spiral-in phase with the orbital period significantly decreasing. The outcome of this scenario cannot

be predicted at this time.

To investigate in more detail the final phase in the lives of our stars, and to establish evidence for any of these three scenarios, we continued several of our models beyond the endpoint of our regular grid (see Sect. 2.2 for details). All models that we evolved further, developed significant envelope instabilities during the final stages of their evolution (case ABC or BBC), leading to high mass transfer rates. While the reliability of these high rates can be questioned, the behavior itself is characterized by periodic variations in luminosity, stellar radius and hence mass loss rate, and has many similarities with the instabilities observed in models of red super giants (Heger et al. 1997). This final mass loss episode is very short and removed all or almost all of the remaining helium envelope, leaving a bare CO shell around a massive ONe core. The period of the oscillations we found is in the order of 4-8 years, which is in good agreement with the findings of Yoon & Cantiello 2010; Paxton et al. 2013. However, the instabilities can have either a physical or numerical origin (Lau et al. 2012), and assessing their validity necessitates a comprehensive resolution study, requiring a substantial number of models each consisting of a large number of time steps. As this kind of resolution study is outside the scope of this paper, we recomputed the late stages of several of our primaries by taking them outside of the binary and including an artificial viscosity term which allows for damping of the pulsations (Paxton et al. 2015). We also applied several different fixed mass loss rates to the models, to simulate a variety of possible mass transfer rates that could be attained in this final RLOF episode. All of these models, however, also ran also into instabilities, albeit at a higher density than the instabilities that occurred when they were still in the binary. Although we got an indication of their subsequent evolution, we were not able to follow the core evolution all the way to high enough densities for the onset of the URCA process or electron captures to be found.

Fig. 9 shows the evolution of two identical cores in a $\rho_c - T_c$ diagram, one with a fixed mass loss rate of $\dot{M} = 10^{-3} M_\odot/\text{year}$ and the other with $\dot{M} = 10^{-9} M_\odot/\text{year}$. The dashed lines are lines of constant neutrino cooling timescales, calculated using the pyMESA package (Farmer 2017). As can be seen, the model with a high mass transfer rate of $\dot{M} = 10^{-3} M_\odot/\text{year}$ continues its cooling trend, as it loses its entire envelope and even eroding the core, preventing any further core growth and possible ensuing contraction. This led to a massive ONe WD with a mass of $1.42 M_\odot$. The model with a low mass transfer rate of $\dot{M} = 10^{-9} M_\odot/\text{year}$ slows down its cooling and gives an indication that it might converge onto a common $\rho - T$ line (Paczynski 1971, Nomoto 1984, 1987 and also observed in Fig. 4 in Takahashi et al. 2013),

somewhere between the $\tau_\nu = 10^4$ yr and $\tau_\nu = 10^5$ yr line. The expectation is that this model will continue to contract, reaching higher and higher densities, aided by the URCA process, eventually leading to conditions that are conducive for electron captures to occur. This path will depend on the core growth rate, as argued by Brooks et al. (2016), and only detailed stellar models, which are able to avoid the discussed envelope instabilities, will provide us with clarity regarding this scenario.

As this scenario is the only course of events that will lead to an ECSN, we will adopt this to determine the initial conditions of close binaries that will produce ECSN. As the Chandrasekhar mass forms the mass limit for stable white dwarfs, we could take $M_{\text{Ch}} = 1.4 M_\odot$ as the lowest possible mass for ECSN. However, our models do not give any indications that cores between $1.38 M_\odot$ and $1.4 M_\odot$ could not undergo this scenario, so in the most optimistic case, the minimum M_{CO} for ECSN is $1.38 M_\odot$, identical to the canonical limit for ECSN in single stars. The upper mass limit for ECSN is given by $M_{\text{CO}} = 1.52 M_\odot$, as argued in Sec. 4.2.

6. PROGENITOR STRUCTURE

The progenitor structure provides significant information regarding the explosion dynamics and the weak and nuclear reactions which can occur in the event of a supernova explosion. The top four panels in Fig. 10 show the chemical structure of our Case A model (Sec. 3.1) and our early and intermediate Case B models (Sec. 3.2). In addition we also provide the chemical structure of a model with a super-Chandrasekhar CO core ($M_{\text{CO}} = 1.51 M_\odot$), which evolved from the initial parameters $M_1 = 15.0 M_\odot$, $M_2 = 12.0 M_\odot$, $P_{\text{init}} = 9$ days and $\beta = 0.5$. All models show a ONe core with a small amount of Mg. The ^{12}C layer is very thin and forms the transition from the dense core to the low density envelope. The density structure is shown in the bottom two panels and shows a steep density gradient at the transition from the core to the envelope. This steep gradient resembles the steep gradient that is characteristic of SAGB models (c.f. Jones et al. 2013, Fig. 7). Temperature profiles are also plotted and show an off-center temperature maximum at a radial mass coordinate close to the carbon burning shell (indicated with a green diamond), indicating that the entire core is cooling.

If these cores are able to explode, the steep density gradients separating the core and the envelope will give rise to a relatively weak and fast explosion, producing a small natal kick, compared to the large natal kick (in the order of 400-500 km s $^{-1}$) experienced after stronger and slower CCSN (Kitaura et al. 2006; Janka et al. 2012; Janka 2017). This dichotomy between small and large natal kick could possibly explain the bimodal distribution in spin period and orbital eccentricity of X-ray bina-

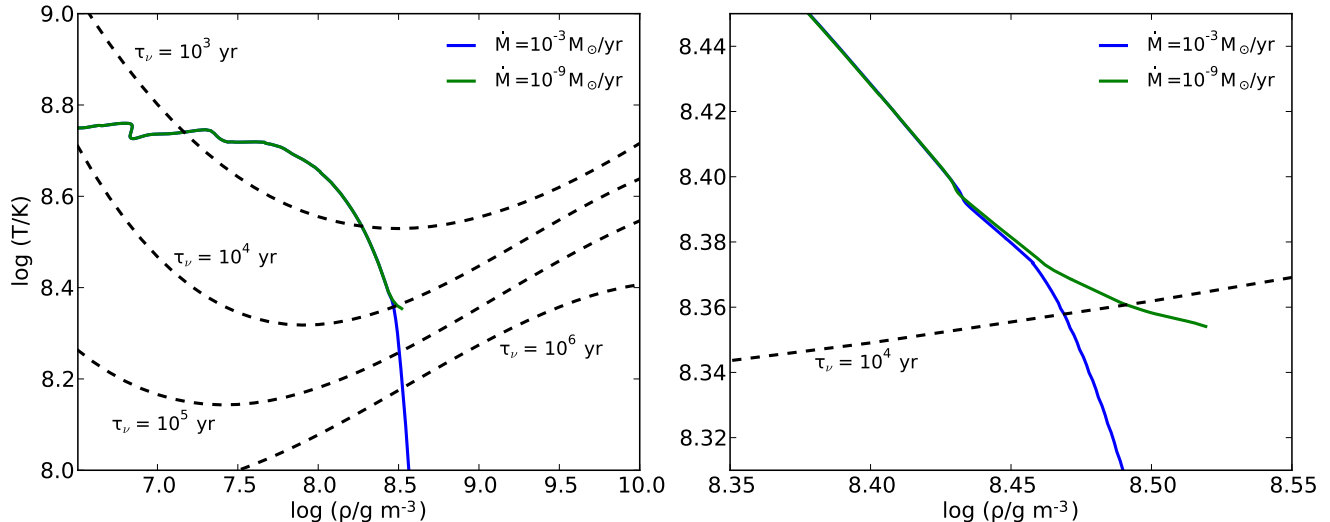


Figure 9. Evolution of the ONe core in the $\rho_c - T_c$ -plane. The right panel is a zoom in of the relevant part of the left panel. The solid lines represents models with a constant mass loss rate of $\dot{M} = 10^{-3} M_{\odot}/\text{yr}$ (blue line) and $\dot{M} = 10^{-9} M_{\odot}/\text{yr}$ (green line). The dashed lines indicate constant neutrino cooling timescale, with values given in the figure. The model with the low mass loss rate (green line) shows a hint of converging onto a common $\rho - T$ line where neutrino cooling and heating due to gravitational contraction are in balance.

ries (Podsiadlowski et al. 2004; Knigge et al. 2011). It is also relevant in the context of double neutron star mergers, where the system remains bound even after experiencing two supernova explosions. This requires at least a small kick in the second supernova, but possibly also significantly smaller kicks in the first supernova, which appears at least possible given the density structure of our models (Beniamini & Piran 2016; Tauris et al. 2017).

7. THE MASS RANGE FOR ECSN

Based on our results described above, we are now in the position to discuss the parameter space where conditions for ECSN are favorable. A total of approximately 45,000 binary sequences were calculated to investigate the ECSN channel in binary stars. A small fraction of the models (approximately 2000) the majority with initial conditions that bring them close to evolving into a contact system, suffered numerical instabilities during their evolution and were terminated because of that. These models were ignored in the final analysis. Most models, however, capture the evolution of the stellar models through carbon burning and the formation of an ONe core, unless the system developed contact. The final fate of our models can therefore be characterized by six different outcomes, which are summarized below and shown in Fig. 11 for one particular combination of parameters, i.e. $\beta = 0.5$ and $q = 0.7$. The full grid is shown in Fig. 12 and will be discussed in more below.

- (Short-P-contact) Models with a short initial period ($P_{\text{init}} \lesssim 2.5$ days at $q = 0.9$ and decreasing to

$P_{\text{init}} \lesssim 1.5$ days at $q = 0.7$) will develop a contact system as the primary fills its Roche lobe during the main sequence and subsequent mass transfer shrinks the orbit so much that also the secondary fills its Roche lobe and contact ensues. These models are not shown in Fig. 11, but the results agree with Wellstein et al. (2001).

- (Long-P-contact) Binary systems with a long initial period will develop contact as well, due to the high mass transfer rates which prevent the secondary to adjust sufficiently fast enough to avoid filling its Roche lobe (indicated with yellow symbols). The late Case B model described in Sec. 3.2 is part of this class.
- (ONe WD) Models with a low initial primary mass ($\lesssim 13.5 M_{\odot}$) will develop a massive ONe WD (indicated with green symbols).
- (CCSN) Models with a high initial primary mass ($\gtrsim 15.2 M_{\odot}$) will develop neon burning and will evolve toward a CCSN (indicated with red symbols).
- (Case B ECSN) Models with a period between ~ 4 days and an upper bound that depends on the values of β and q and initial primary masses of $\sim 13.5 - 15.2 M_{\odot}$ develop Case B mass transfer and a CO core that falls with a mass between $1.37 M_{\odot}$ and $1.52 M_{\odot}$ (indicated with blue symbols, ECSN - Case B).

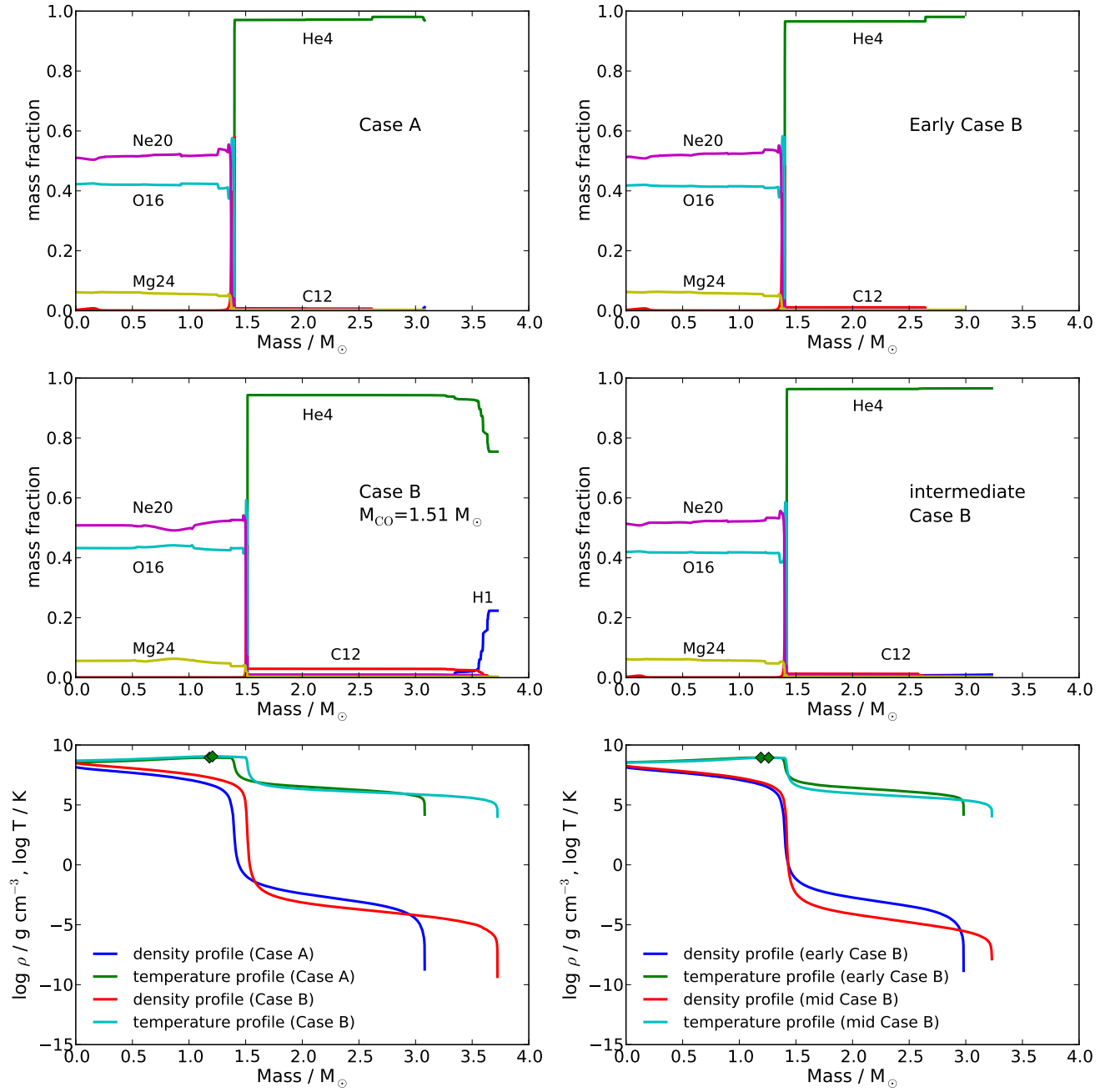


Figure 10. Progenitor structure of four different models. The top rows show the chemical structure as a function of the mass coordinate. The bottom row shows the temperature and density structure of the progenitor model as a function of mass coordinate. All models possess an ONe core, with a fraction of Mg. The structure resembles that of a single SAGB star with a sharp density gradient separating the core from the envelope, c.f. Jones et al. 2013, Fig. 7. The temperature profiles show an off-center maximum, marked with a green diamond.

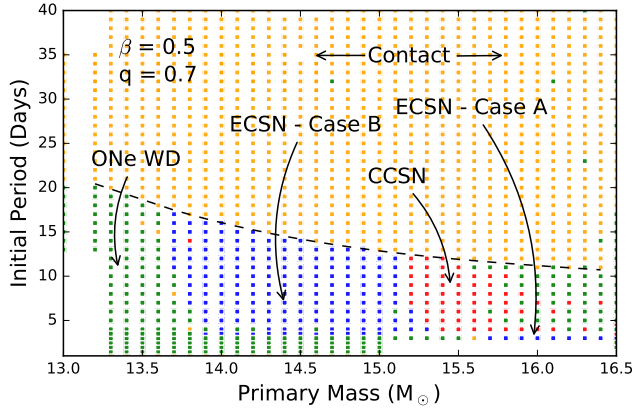


Figure 11. Expected final fate of computed models in our grid for $\beta = 0.5$ and $q = 0.8$ as a function of initial primary mass and initial period. Five distinct outcomes are visible and labeled. ECSN are indicated by blue dots.

- (Case A ECSN) Models with an initial period that is between ~ 2.5 and ~ 3.5 days (depending on the value of q) will develop late Case A mass transfer. As the development of the helium core is significantly hampered by this mass transfer, the primary initial mass range shifts to higher initial masses with respect to Case B systems (indicated with blue symbols, ECSN - Case A).

In Fig. 11 we show these final evolutionary outcomes for a particular combination of parameters, i.e. $\beta = 0.5$ and $q = 0.7$ (compare also with Wellstein et al. 2001, Fig. 12). As argued above, while in single stars CO cores with masses between $1.37 M_{\odot}$ and $1.42 M_{\odot}$ will result in an ECSN, in binary stars these ranges could possibly be as wide as $1.37 - 1.52 M_{\odot}$. ECSN progenitors have a minimum mass of $13.7 M_{\odot}$ which increases to $13.9 M_{\odot}$ for early Case B systems (analogical to the much larger shift in initial mass for Case A systems). The upper mass limit for ECSN progenitors is found at $15.1 M_{\odot}$ with a slight shift to higher initial masses ($15.3 M_{\odot}$) for early Case B systems. This boundary forms the transition to progenitors that develop neon burning. Case A ECSN progenitors can be found at $P_{\text{init}} = 3$ days, between $M_1 = 15.7 M_{\odot}$ and $M_1 = 16.4 M_{\odot}$. For this particular combination of q and β , the minimum period for systems to develop contact decreases from about 20 days at $M_1 = 13.5 M_{\odot}$ to ~ 10 days at $M_1 = 16.5 M_{\odot}$. This limits the number of ECSN candidates at higher initial masses, but also the progenitors that develop neon burning.

Plotted in Fig. 12 are all ECSN and CCSN progenitors (respectively red crosses and blue crosses) in our entire parameter space as a function of initial primary mass and initial period, with four different values of the mass ratio q plotted horizontally ($q =$

$0.6, 0.7, 0.8, 0.9$), and four different values of β plotted vertically ($\beta = 0, 0.25, 0.5, 0.75$). The approximate boundary between contact and contact-free systems is indicated by a dashed line. This line is a third order polynomial fit to the maximum contact-free period, and hence should be taken as an approximation. M_{CO} between $1.37 M_{\odot}$ and $1.52 M_{\odot}$ are indicated with contour lines at $M_{\text{CO}} = 1.4, 1.43, 1.46, 1.49 M_{\odot}$.

As can be seen, most combinations of q and β behave qualitatively similar, especially with respect to the position of the initial mass limits for ECSN, although the boundaries between contact systems and non-contact systems shift for various combinations of q and β . A general trend (except for $\beta = 0.75$ with $q = [0.7, 0.8, 0.9]$) can be seen such that for lower initial primary masses contact-free systems can be found toward longer initial periods. This is the result of lower mass transfer rates due to RLOF at lower masses (c.f. Fig. 4), which allows the secondary to adjust to the mass accretion, instead of overflowing its Roche lobe. For lower values of q (i.e. a larger difference between the initial primary and secondary mass) we see the boundary between contact and non-contact systems shift to shorter period. As the mass difference is larger for low q , the size of the Roche lobe of the secondary is smaller, and once mass transfer starts, it is easier for the secondary to fill the Roche lobe and develop contact. This effect is stronger for more efficient mass transfer, as it is more difficult for the secondary to adjust its radius in response to the larger amounts of accreted mass. As can be seen in Fig. 12, upper left corner, systems with $q = 0.6$ and $\beta = 0, 0.25$ all develop contact. A clear trend is visible for less efficient mass transfer toward more contact-free systems at long periods. As more matter leaves the system, less matter is accreted onto the secondary, which does not fill its Roche lobe until longer periods.

For most combinations of q and β , the initial primary mass for ECSN is confined to a narrow range between $13.6 M_{\odot}$ and $15.1 M_{\odot}$ for Case B systems and between $15.5 M_{\odot}$ and $17.6 M_{\odot}$ for Case A. For fully conservative evolution ($\beta = 0$) the initial periods for systems Case B mass transfer that result in an ECSN are confined to $P_{\text{init}} < 10$ days and mass ratios $q > 0.75$. Several Case A systems are found for initial primary masses between $15.8 M_{\odot}$ and $16.4 M_{\odot}$ at a period of 3.5 days. All Case B systems for mass ratios below 0.7 develop contact, however, there are Case A systems with an initial period of 3 days and initial primary masses between $15.8 M_{\odot}$ and $16.3 M_{\odot}$. This is in good agreement with Wellstein et al. (2001) who find that Case A systems avoid contact for lower q compared with Case B systems.

For non-conservative evolution the mass range for ECSN barely changes, however, the range in initial periods does increase. For $\beta = 0.25$ (25% of the mass

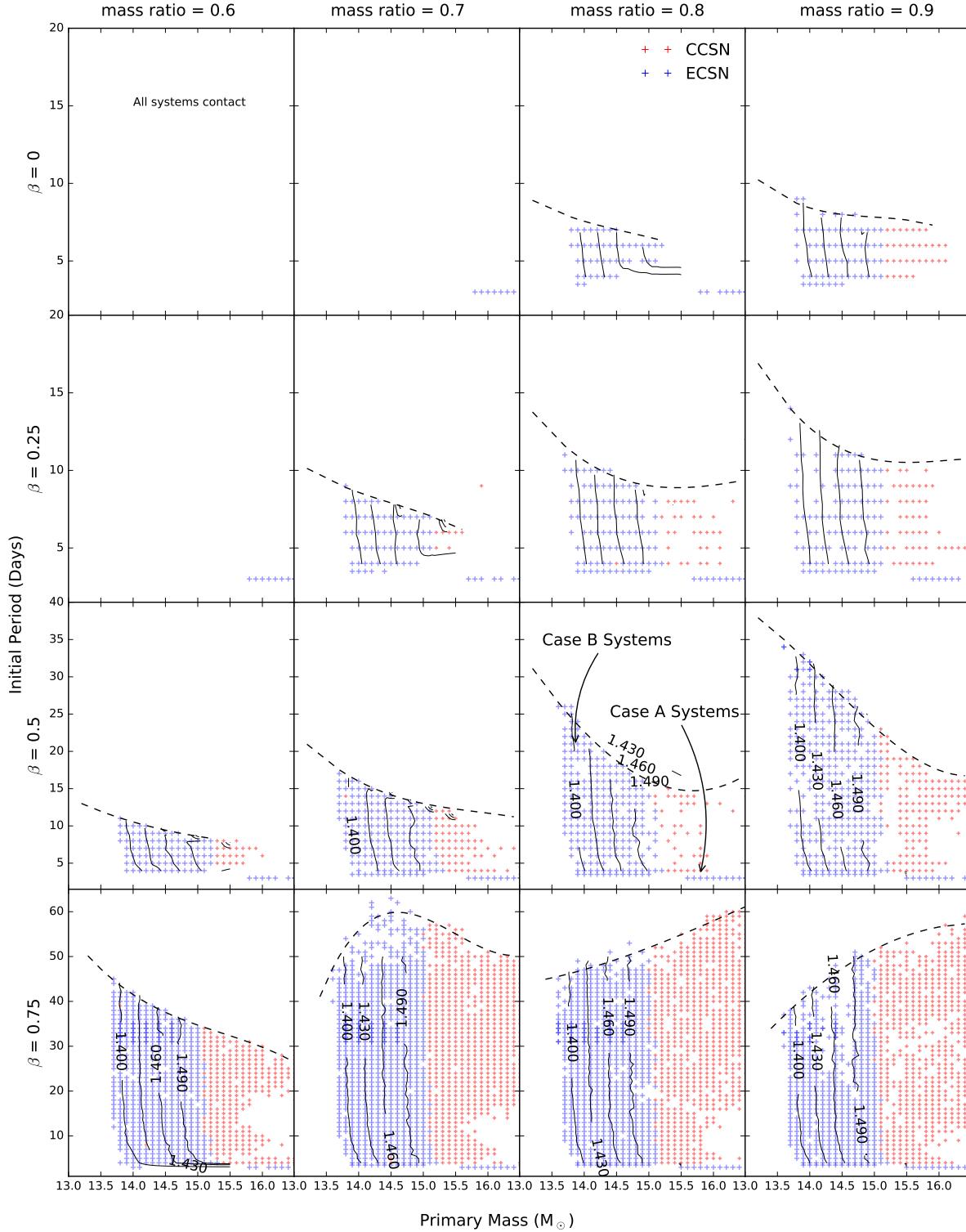


Figure 12. ECSN (blue) and CCSN models (red) as a function of initial primary mass and initial period, for $\beta = 0, 0.25, 0.5, 0.75$ and mass ratios $q = 0.6, 0.7, 0.8, 0.9$. The initial period for the two top rows is limited to 20 days, and the third row to 40 days as systems with larger periods evolve all to contact binaries. Case A and Case B systems are indicated in the panel for $(q, \beta) = (0.8, 0.5)$ and are representative for all other panels. Masses of the pre-ECSN CO cores are indicated with contour lines, marking the location of 1.40, 1.43, 1.46, and 1.49 M_{\odot} . The approximate boundary between contact and contact-free systems is indicated by a dashed line.

lost from the primary star is expelled from the system) the maximum period increases to about ~ 15 days for a mass ratio near unity and decreases to 10 days for a mass ratio of 0.70.

For non-conservative evolution with $\beta = 0.5$ (50% accreted, 50% expelled) the maximum initial period for Case B systems increases to 33 days for $q = 0.9$, to 25 days for $q = 0.8$ and to 17 days for $q = 0.7$. The systems discussed in Section 3 are part of this data set. Case A mass transfer leading to ECSN occurs for all mass ratios, while Case B mass transfer is still limited to $0.7 < q < 1$.

The situation for the non-conservative case with $\beta = 0.75$ (75% expelled, 25% accreted) is a bit different as the maximum period for ECSN formation increases from 50 days in the $q = 0.9$ case to 57 days in the $q = 0.7$ case. Models with a value of $\beta = 0.75$ form the only instance for $q = 0.6$ that shows ample evidence for Case B systems able to evolve to a ECSN. These Case B systems are found between $13.7 M_{\odot}$ and $15.0 M_{\odot}$ with an initial period between 4 days and 45 days.

8. DISCUSSION AND CONCLUSIONS

We have presented models of close binary systems where the primary star could potentially be the progenitor of an ECSN. While the mass range for ECSN in single stars is fairly narrow (Poelarends et al. 2008), the mass range for ECSN in binary stars is thought to be much wider as the effects of mass loss due to Roche lobe overflow are thought to mitigate the effects of the second dredge-up in single stars (Podsiadlowski et al. 2004). In single stars, this second dredge-up reduces the mass of the helium core below the Chandrasekhar mass (in the relevant initial mass range) and makes that the possibility for an ECSN depends on the outcome of the race between core-growth and envelope mass loss during the SAGB (Poelarends et al. 2008; Takahashi et al. 2013). If the core is able to contract to high enough densities so that electron captures on ^{24}Mg and ^{20}Ne can commence, heating as a result of these electron captures will cause O+Ne burning at the center, and O+Ne deflagration propagates outward. Core contraction is further accelerated by electron captures in the central nuclear statistical equilibrium region, resulting in a weak Type II supernova (Takahashi et al. 2013; Kitaura et al. 2006). However, if mass loss removes the envelope fast enough so that the core is not able to reach those critical densities, the star will evolve into a massive ONe white dwarf.

Our study, however, has focused on binary systems instead of single stars and attempts to answer two major questions concerning: First, are binary systems indeed capable of producing and ECSN, and, second, what is the expected region in the $(M_1, M_2, P_{\text{init}})$ phase space that we can expect these ECSN to occur? We have investigated these questions by running approximately

45,000 binary models in the relevant phase space.

8.1. The Possibility of ECSN from Close Binary Systems

Based on single star models there is consensus in the literature that a star will experience an ECSN when M_{CO} is somewhere between ~ 1.37 and $\sim 1.42 M_{\odot}$ (see for example Woosley & Heger 2015; Tauris et al. 2015; Moriya & Eldridge 2016, who all adopt similar values). Tauris et al. (2015), in the context of ultra-stripped supernovae, use as a “rule of thumb” (based on single star models) that the upper boundary for ECSN is given by stars that develop a post-carbon burning central temperature above their carbon burning central temperature as these conditions will lead to an iron core collapse. In this case the ignition of neon and oxygen burning will eventually convert the composition of the entire core into ^{28}Si and ^{32}S , bringing the chance for contraction due to electron captures to an end. Their lower boundary is given by the ONe WD threshold of $1.37 M_{\odot}$, as these cores are not able to contract to sufficiently high densities where electron captures can commence.

Based on the models presented above, however, we question whether these boundaries can be applied to stars in a binary system, as mass loss driven by Roche lobe overflow, especially after central carbon burning drives the star out of thermal equilibrium, leading to significant expansion and a much stronger cooling in the core than in single stars. While in single stars the effect of neutrino cooling is compensated by heating due to core growth, keeping the central temperature of the star roughly constant during the post-carbon burning contraction (Nomoto 1984), in binary stars the cooling is enhanced by mass loss. However, if cooling due to thermal neutrino losses and heating due to gravitational contraction come into equilibrium as argued in Sec. 5, the central conditions will eventually follow a common evolutionary track in the $\rho_c - T_c$ plane and the core will be able to evolve to conditions that are conducive for electron captures to commence. Nevertheless, many ingredients for this contraction are different from the evolution of single stars, and a simple comparison of single and binary evolutionary tracks in the $\rho_c - T_c$ plane to deduce their final fate is not possible. This scenario would apply to all cores that do not ignite neon ($M_{\text{core}} \lesssim 1.52 M_{\odot}$) down to the effective Chandrasekhar mass ($\sim 1.40 M_{\odot}$) or possibly even $\sim 1.37 M_{\odot}$ and deserves further investigation.

In case the primary star loses its entire envelope and is not able to contract to densities high enough for electron captures to commence, there is still an alternative scenario that could lead to an ECSN. Once the secondary leaves the main sequence, its expansion will give rise to reverse Roche lobe overflow (De Donder & Vanbe-

eren 2003; Zapartas et al. 2017). This will likely happen not immediately, as the binary separation has grown to $\sim 1000 R_{\odot}$. Eventually, however, only a tiny bit of mass accretion onto the ONe white dwarf will heat up the cold white dwarf, allow core growth to resume, reheat the core and possibly give rise to conditions that are conducive for electron captures to accelerate the heating process. This will ultimately, although delayed compared with the direct explosions described above, result in the collapse of the core and the formation of a neutron star (Nomoto 1984; Dessart et al. 2006; Schwab et al. 2016).

8.2. Comparison with Previous Work

The results presented in this paper differ significantly from earlier studies that evaluated the existence of ECSN in binary systems. The first paper to discuss such supernovae in binaries was Podsiadlowski et al. (2004) who concluded that, based on models by Wellstein et al. (2001), initial primary masses between $8 M_{\odot}$ and $17 M_{\odot}$ would be expected to evolve into an ECSN. This estimate was based on the helium core criterion developed by Nomoto (1984) who showed that helium cores between $2 M_{\odot}$ and $2.5 M_{\odot}$ lead to conditions where electron captures will kick off the collapse of the core.

Despite the differences, many of the fundamental ideas in Podsiadlowski et al. (2004) are confirmed by this paper. While their inference was based on only a handful of models that established the relationship between the initial mass and final helium mass of stars in close binary systems, our detailed grid confirms indeed that the spread in M_{CO} is fundamentally a result of the period, and that the difference in timing of Roche lobe overflow between Case A and Case B systems will result in Case A systems developing smaller cores, effectively shifting their initial mass-final core mass relationship toward higher initial masses.

Our research, however, provides several improvements on Podsiadlowski et al. (2004). First of all, the helium core criterion, developed by Nomoto (1984) might work well for single stars, it, however, gives less accurate results for binary stars. The main reason for this is that primaries in close binary systems suffer from significant mass loss due to RLOF, either during the main sequence or in the Hertzsprung gap, which considerably affects the development and mass of the helium core, either directly by erosion, or indirectly through the adjustment of the star to mass transfer. Although the CO core is not directly affected (i.e. eroded) by mass transfer due to RLOF, there is still an appreciable difference between the evolution of CO cores of the same mass in single stars and in binary systems, as Fig. 8 shows. Secondly, whereas Podsiadlowski et al. (2004) expected that mass loss due to Roche lobe overflow would prevent the second

dredge-up from happening, we find that mass loss actually has a very similar effect in reducing the mass of the helium core. Indeed, the second dredge-up was avoided, but the mass of the hydrogen envelope and sometimes the underlying helium layer was significantly reduced. Evidence for this erosion of the helium layer was already present in Wellstein et al. (2001), however, it was not considered in Podsiadlowski et al. (2004). Third, our models show that the role of mass loss in the final evolution toward electron captures is much larger than was previously thought. Cores undergoing significant mass loss compensate for this by expansion and enhanced cooling. This leads to massive ONe cores (up to $\sim 1.52 M_{\odot}$) that are able to avoid neon ignition. If the ONe core is able to contract to high enough densities to cause the conditions for electron captures to occur we expect a maximum mass range for Case B systems that is $\sim 2 M_{\odot}$ wide and a maximum mass range for Case A systems that is $\sim 3 M_{\odot}$ wide. When we combine both mass ranges, the maximum mass range for ECSN from binary systems runs from an initial primary mass of $\sim 13.5 M_{\odot}$ to $\sim 18 M_{\odot}$, a width of $\sim 4.5 M_{\odot}$, which is significantly narrower than the prediction of Podsiadlowski et al. (2004) but much wider than the initial mass range for single stars (roughly $0.25 M_{\odot}$, Poelarends et al. 2008). The use of a different convection criterion (e.g. Schwarzschild instead of Ledoux, more efficient semi-convection, or additional convective boundary mixing), will translate the mass range to lower values (possibly somewhere around $\sim 10 - 15 M_{\odot}$), without affecting the primary conclusions of this paper (c.f., Appendix A, Doherty et al. 2010). This will be further explored in a future publication. Even so, the improvements of the models that we have presented there provide a picture that makes the possibility for ECSN from close binary systems much less likely than originally thought.

Our models are in broad agreement with the results of Tauris et al. (2013, 2015). While their research is focused on helium cores orbiting a compact object, the general evolutionary picture shows lots of similarities (compare Fig. 18 in Tauris et al. 2015 with our Fig. 12). As it is not clear which role mass loss plays in their models, especially during and after carbon burning, we don't know whether our results are applicable to their situation. Regardless, more research is needed to accurately describe the evolution of massive ONe cores at high densities, whether they converge onto a common evolutionary track in the $\rho_c - T_c$ plane and are able to contract to sufficiently high densities for electron captures to destabilize the core, or that they continue to cool down and avoid electron captures all together. Much of this will determine the exact mass range of ECSN in binary systems as neither the mass of the CO core, nor the track in the $\rho_c - T_c$ plane, are, according to our models, sufficient

to uniquely determine the final fate of these stars.

8.3. The Expected Initial Mass Range for ECSN in Close Binary Systems

If we assume that continued core contraction after mass loss ceases will eventually converge the evolution a core onto a common evolutionary track in the $\rho_c - T_c$ plane toward electron captures, we are able to characterize, within the limits of our assumptions on the treatment of convection, overshooting, mixing, and accretion, the initial mass range for ECSN. Figure 13 provides a different way of looking at our dataset, showing the final M_{CO} as a function of the initial primary mass. The horizontal dashed red line at $1.52 M_\odot$ indicates the maximum M_{CO} that avoids neon ignition, and hence forms the upper boundary of the ECSN range. This upper boundary could be shifted to even higher M_{CO} if neon flames are able to stall (Jones et al. 2014), leaving the chemical composition in the center unaltered and allowing for subsequent electron captures to occur. Most work on stalling flames has been done in the context of carbon flames by Denissenkov et al. (2013, 2015); Farmer et al. (2015) whose research suggest that efficient convective boundary mixing can disrupt inwardly propagating carbon flames, however Lecoanet et al. (2016) find that hybrid cores are unlikely. We defer to future work the investigation of quenched neon flames which might influence our upper boundary for M_{CO} leading to ECSN. The horizontal dash-dotted green line at $1.4 M_\odot$ indicates the Chandrasekhar mass for a composition of 50% neon and 50% oxygen. The horizontal dashed red line at $1.37 M_\odot$ indicates the lowest possible CO core mass that is able to evolve into an ECSN.

Two distinct sequences are visible in each panel (cf. Wellstein & Langer 1999, Fig 5b), Case B models (on the left) and Case A models (on the right). The reason that Case B and Case A systems are separate is that mass loss during the main sequence reduces the hydrogen burning core, effectively shifting the ECSN range for Case A systems to higher initial masses. The scatter in the vertical direction can be attributed to a spread in initial period, with models toward the lower end of the sequence originating from low period binaries, while models toward the higher end of the sequence originating from higher period binaries, giving rise to smaller, resp. larger CO cores (c.f. the discussion in Section 3, see also Wellstein et al. 2001). As argued in Sec. 7, initial periods that are longer than our ECSN candidates lead to contact systems, while initial periods that are shorter than our ECSN candidates lead to either a CO core below the critical mass for neon ignition, or to a Case A contact system. Thus it appears that for a given initial primary mass the initial period will allow for a certain spread in final M_{CO} . However, the key factor that determines

the location of the ECSN channel is the initial primary mass. While the number of models that are able to produce CO cores that are favorable for the development ECSN increases with increasing β the ECSN mass range itself does not really shift. This is true for both the Case A ECSN channel as for the Case B ECSN channel. If we allow all CO cores with $1.37 M_\odot \leq M_{\text{CO}} \leq 1.52 M_\odot$ to eventually explode as an ECSN we find an initial mass range for ECSN between $13.5 M_\odot$ and $15.25 M_\odot$ for Case B systems and between $15.4 M_\odot$ and $17.6 M_\odot$ for Case A systems. This mass range is indicated in Figure 13 with arrows marked “Case B – max” and “Case A – max”, respectively. If we confine the cores that are able to evolve into an ECSN to M_{CO} between the Chandrasekhar mass ($1.40 M_\odot$) and $1.52 M_\odot$ the initial mass range for ECSN narrows to $14.2 M_\odot$ and $15.25 M_\odot$ for Case B systems and between $16.1 M_\odot$ and $17.6 M_\odot$ for Case A systems. This mass range is indicated in Figure 13 with arrows marked “Case B – min” and “Case A – min”, respectively. Both channels are slightly offset from the single star ECSN channel, which, for the chosen input physics and convection criterion, is located between $12.7 M_\odot$ and $13.2 M_\odot$, based on $1.38 M_\odot \leq M_{\text{CO, single}} \leq 1.42 M_\odot$. This difference in initial masses is small and probably difficult to detect observationally in a population consisting of both single and binary stars. As our input physics in terms of convective mixing is similar to Wellstein et al. (2001), i.e. we don’t take into account additional mixing such as convective overshooting or exponentially decreasing diffusion Herwig (2000), we expect that this initial mass range might shift to lower initial masses by $2 - 3 M_\odot$ if additional mixing is taken into account. It should, however, not have significant effects on the evolution or the structure of the models or any of our further conclusions (see App. A).

It is worth noting that more ECSN are predicted for systems with a mass ratio close to unity, as the development of contact happens at longer period for higher q systems (see Fig. 12). As the primary star starts transferring mass to the secondary, the orbit shrinks, until the mass ratio is reversed. This reversal happens earlier for mass ratios close to one, and later for lower mass ratios, increasing the chance for contact (de Mink et al. 2013). This primarily affects the numbers of ECSN, not so much the initial mass range (except for Case A systems). This is also true for the value of β , which controls the amount of matter that is lost from the system (i.e., $\beta = 0$ is conservative mass transfer, no mass that is transferred from the primary to the secondary is lost from the system; $\beta = 1$ is completely non-conservative mass transfer, all mass that is transferred from the primary is lost from the system, no accretion onto the secondary). For the sake of our parameter study we chose various fixed values of β , while the mass transfer effi-

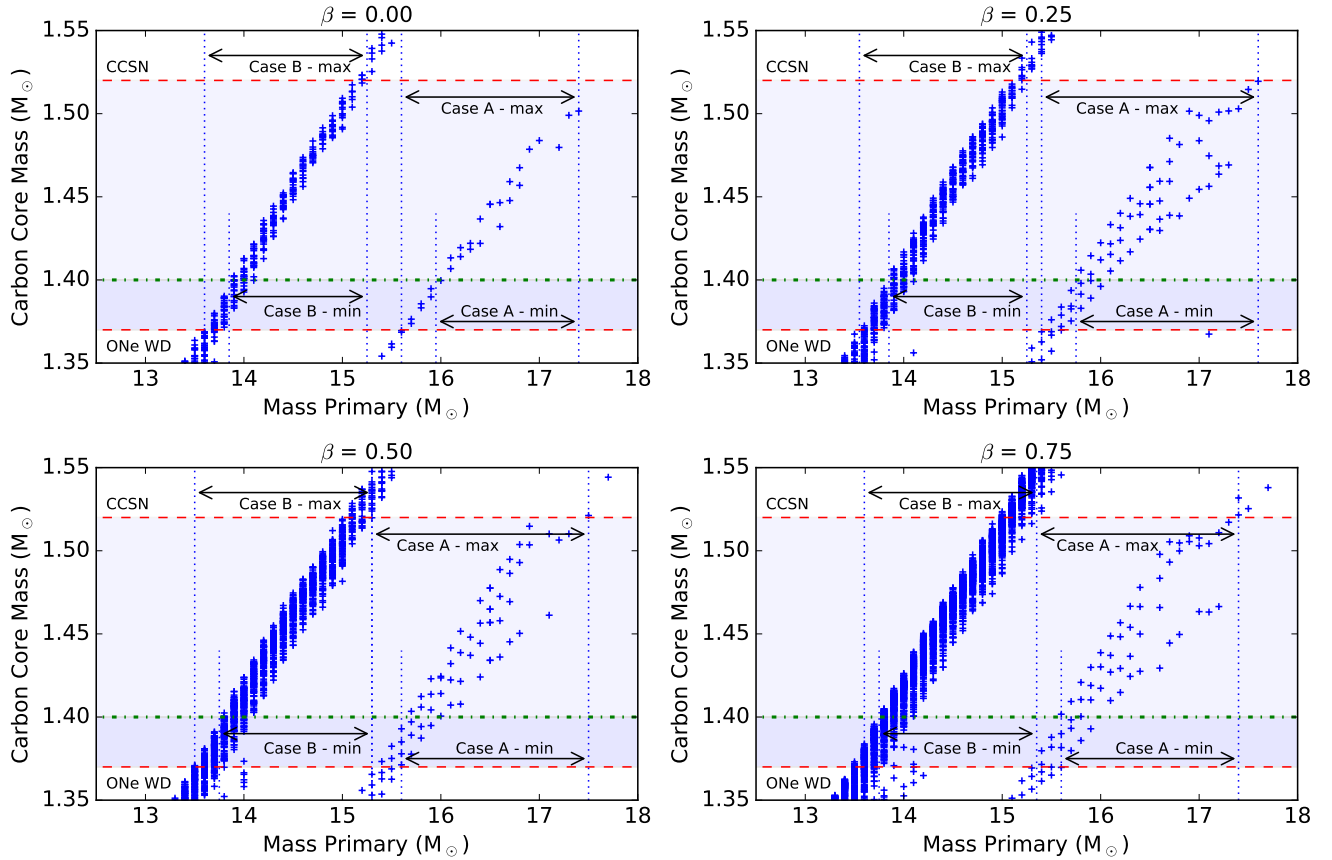


Figure 13. Final M_{CO} as a function of initial mass, organized by mass transfer efficiency (β) in four panels. The horizontal dashed red at $1.52 M_{\odot}$ indicates the maximum possible M_{CO} that does not lead to off-center neon ignition, and thus forms the upper boundary of the ECSN range. The horizontal dash-dotted green line at $1.4 M_{\odot}$ indicates the effective Chandrasekhar mass. The horizontal dashed red line at $1.37 M_{\odot}$ indicates the lowest possible CO core mass that might be able to evolve into an ECSN. The light shaded area between $1.37 M_{\odot} \leq M_{\text{CO}} \leq 1.52 M_{\odot}$ and $1.4 M_{\odot} \leq M_{\text{CO}} \leq 1.52 M_{\odot}$ indicates the maximum and most feasible ECSN range, as long as the decrease in temperature is stopped and the density is able to increase again.

ciency in real systems varies in time and will depend on the evolutionary phase of both stars, the amount of matter already accreted onto the secondary and how that has affected its spinrate. Several mechanisms have been suggested which control the efficiency of mass transfer, mass accretion and mass loss, including the existence of an accretion disk that regulates the amount of mass and angular momentum that can be accreted (Paczynski 1991; Popham & Narayan 1991; Deschamps et al. 2013), the necessity of the secondary to stay below critical rotation (Packet 1981), and the effects of tides on the stellar spins and the stellar orbit (Zahn 1977; Hurley et al. 2002). Work by Deschamps et al. (2013); van Rensbergen et al. (2008) for systems with slightly lower masses suggests periods with values of β close to 1 (i.e. very inefficient mass transfer), while simulations with a strong tidal interaction (i.e. a short spin-orbit synchronization timescale) suggest shorter periods of moderately inefficient mass transfer (Paxton et al. 2015). Although our models suggest that the efficiency of mass trans-

fer does not really affect the mass range for ECSN, it does, however, strongly affect the range of initial periods that can lead to an ECSN. In addition, the evolution of the secondary will be affected. It will most likely rapidly spin up after the onset of mass transfer and maintain near-critical rotation for possibly extended periods of time. This will induce strong rotational mixing (Langer 2012; de Mink et al. 2008a, 2013), causing possibly quasi-chemically homogeneous evolution (Maeder 1987; Langer 2012) and alter the evolution of the star beyond just the simple fact of mass accretion (Hirschi et al. 2004; de Mink & Mandel 2016; Marchant et al. 2016). Although it is not clear to what extent this will affect the incidence of ECSN, the effects of tides, mass and angular momentum transfer and loss, and near-critical rotation of the secondary are possibly important and will be discussed in a forthcoming paper, in addition to the effects of additional mixing and convection criteria.

If the scenario for the formation of ECSN in binaries, as discussed in this paper, turns out to correct,

the binary ECSN channel might contribute to the population of NS+NS systems that can be observed with aLIGO/Virgo (Côté et al. 2017). Precursors to these NS+NS systems will be visible as Be/X-ray binaries (Knigge et al. 2011; Shao & Li 2014). With the discovery of GW170817 (The LIGO Scientific Collaboration et al. 2017a), electron-capture supernovae have been propelled into the spotlight (The LIGO Scientific Collaboration et al. 2017b). As the progenitors of NS+NS collisions have to survive two supernova explosions, while still remain bound, ECSN are promising candidates as the NS kick is expected be much smaller for ECSN than for CCSN (Podsiadlowski et al. 2004). While our research has focused on the first supernova in a binary system, low natal kicks from ECSN are particularly relevant in the second explosion (Tauris et al. 2017). However, our conclusion that CO cores with masses up to $1.52 M_{\odot}$ can produce ECSN is potentially relevant in determining the final fate of so-called ultra-stripped supernovae, the sec-

ond supernova in a NS+NS system (Tauris et al. 2013, 2015, 2017).

We thank the anonymous referee for very detailed and constructive feedback, which significantly contributed to improving the quality of this paper. We thank Neile Havens for excellent technical support and Harvard Townsend for administrative IT support. AJP acknowledges support from the Aldeen Fund. SW, SH, and JT like to thank Dr. Dorothy Chappell, Dean of Natural and Social Sciences at Wheaton College and the Wheaton College Alumni Association for support for the summer research program. We thank the MESA council for making available, maintaining and continuously developing an outstanding stellar evolution code. This research used the High Performance Computing resources at Wheaton College and also has made use of NASA’s Astrophysics Data System.

Software: MESA (v8118; Paxton et al. 2011, 2013, 2015), pyMESA, Farmer 2017.

REFERENCES

- Abbott, B. P., Abbott, R., Abbott, T. D., Abernathy, M. R., Acernese, F., Ackley, K., Adams, C., Adams, T., Addesso, P., Adhikari, R. X., & et al. 2016, *Living Reviews in Relativity*, 19, 1
- Almeida, L. A., Sana, H., Taylor, W., Barbá, R. , Bonanos, A. Z., Crowther, P., Damiani, A., de Koter, A. , de Mink, S. E., Evans, C. J., Gieles, M., Grin, N. J. a and Hénault-Brunet, V., Langer, N., Lennon, D., Lockwood, S., Maíz Apellániz, J., Moffat, A. F. J. ., Neijssel, C., Norman, C., Ramírez-Agudelo, O. H., Richardson, N. D., Schootemeijer, A., Shenar, T., Soszyński, I., Trammer, F., & Vink, J. S. 2017, *A&A*, 598, A84
- Beniamini, P. & Piran, T. 2016, *MNRAS*, 456, 4089
- Böhm-Vitense, E. 1958, *ZA*, 46, 108
- Brooks, J., Bildsten, L., Schwab, J., & Paxton, B. 2016, *ApJ*, 821, 28
- Côté, B., Belczynski, K., Fryer, C. L., Ritter, C., Paul, A., Wehmeyer, B., & O’Shea, B. W. 2017, *ApJ*, 836, 230
- Das, U. & Mukhopadhyay, B. 2013, *Physical Review Letters*, 110, 071102
- De Donder, E. & Vanbeveren, D. 2003, *NewA*, 8, 415
- de Mink, S. E., Cantiello, M., Langer, N., Yoon, S.-C., Brott, I., Glebbeek, E., Verkoulen, M., & Pols, O. R. 2008a, in *IAU Symposium, Vol. 252, The Art of Modeling Stars in the 21st Century*, ed. L. Deng & K. L. Chan, 365–370
- de Mink, S. E., Langer, N., Izzard, R. G., Sana, H., & de Koter, A. 2013, *ApJ*, 764, 166
- de Mink, S. E. & Mandel, I. 2016, *MNRAS*, 460, 3545
- de Mink, S. E., Pols, O. R., & Hilditch, R. W. 2007, *A&A*, 467, 1181
- de Mink, S. E., Pols, O. R., & Yoon, S.-C. 2008b, in *American Institute of Physics Conference Series, Vol. 990, First Stars III*, ed. B. W. O’Shea & A. Heger, 230–232
- de Mink, S. E., Sana, H., Langer, N., Izzard, R. G. , & Schneider, F. R. N. 2014, *ApJ*, 782, 7
- Denissenkov, P. A., Herwig, F., Truran, J. W., & Paxton, B. 2013, *ApJ*, 772, 37
- Denissenkov, P. A., Truran, J. W., Herwig, F., Jones, S., Paxton, B., Nomoto, K., Suzuki, T., & Toki, H. 2015, *MNRAS*, 447, 2696
- Deschamps, R., Siess, L., Davis, P. J., & Jorissen, A. 2013, *A&A*, 557, A40
- Dessart, L., Burrows, A., Ott, C. D., Livne, E., Yoon, S.-C., & Langer, N. 2006, *ApJ*, 644, 1063
- Doherty, C. L., Gil-Pons, P., Lau, H. H. B., Lattanzio, J. C., & Siess, L. 2014a, *MNRAS*, 437, 195
- Doherty, C. L., Gil-Pons, P., Lau, H. H. B., Lattanzio, J. C., Siess, L., & Campbell, S. W. 2014b, *MNRAS*, 441, 582
- Doherty, C. L., Gil-Pons, P., Siess, L., Lattanzio, J. C., & Lau, H. H. B. 2015, *MNRAS*, 446, 2599
- Doherty, C. L., Siess, L., Lattanzio, J. C., & Gil-Pons, P. 2010, *MNRAS*, 401, 1453
- Doom, C. 1984, *A&A*, 138, 101
- Duchêne, G. & Kraus, A. 2013, *ARA&A*, 51, 269
- Farmer, R. 2017, *rjfarmer/pyMesa v1.0.0*, zenodo, doi:10.5281/zenodo.846305
- Farmer, R., Fields, C. E., & Timmes, F. X. 2015, *ApJ*, 807, 184
- García-Berro, E. & Iben, I. 1994, *ApJ*, 434, 306
- García-Berro, E., Ritossa, C., & Iben, I. J. 1997, *ApJ*, 485, 765
- Grevesse, N. & Noels, A. 1993, *Physica Scripta*, 1993, 133
- Grevesse, N. & Sauval, A. J. 1998, *SSRv*, 85, 161
- Heger, A., Fryer, C. L., Woosley, S. E., Langer, N., & Hartmann, D. H. 2003, *ApJ*, 591, 288
- Heger, A., Jeannin, L., Langer, N., & Baraffe, I. 1997, *A&A*, 327, 224
- Heger, A., Langer, N., & Woosley, S. E. 2000, *ApJ*, 528, 368
- Hellings, P. 1983, *Ap&SS*, 96, 37
- Herwig, F. 2000, *A&A*, 360, 952
- Hicken, M., Garnavich, P. M., Prieto, J. L., Blondin, S., DePoy, D. L., Kirshner, R. P., & Parrent, J. 2007, *ApJL*, 669, L17
- Hirschi, R., Meynet, G., & Maeder, A. 2004, *A&A*, 425, 649
- Hurley, J. R., Tout, C. A., & Pols, O. R. 2002, *MNRAS*, 329, 897
- Iben, I. J., Ritossa, C., & García-Berro, E. 1997, *ApJ*, 489, 772

- Itoh, N., Hayashi, H., Nishikawa, A., & Kohyama, Y. 1996, *ApJS*, 102, 411
- Janka, H.-T. 2017, *ApJ*, 837, 84
- Janka, H.-T., Hanke, F., Hüdepohl, L., Marek, A., Müller, B., & Obergaulinger, M. 2012, *Progress of Theoretical and Experimental Physics*, 2012, 01A309
- Jones, S., Hirschi, R., & Nomoto, K. 2014, *ApJ*, 797, 83
- Jones, S., Hirschi, R., Nomoto, K., Fischer, T., Timmes, F. X., Herwig, F., Paxton, B., Toki, H., Suzuki, T., Martínez-Pinedo, G., Lam, Y. H., & Bertolli, M. G. 2013, *ApJ*, 772, 150
- Kitaura, F. S., Janka, H.-T., & Hillebrandt, W. 2006, *A&A*, 450, 345
- Knigge, C., Coe, M. J., & Podsiadlowski, P. 2011, *Nature*, 479, 372
- Kobulnicky, H. A. & Fryer, C. L. 2007, *ApJ*, 670, 747
- Kobulnicky, H. A., Kiminki, D. C., Lundquist, M. J., Burke, J., Chapman, J., Keller, E., Lester, K., Rolen, E. K., Topel, E., Bhattacharjee, A., Smullen, R. A., Vargas Álvarez, C. A., Runnoe, J. C., Dale, D. A., & Brotherton, M. M. 2014, *ApJS*, 213, 34
- Kudritzki, R. P., Pauldrach, A., & Puls, J. 1987, *A&A*, 173, 293
- Langer, N. 2012, *ARA&A*, 50, 107
- Langer, N., El Eid, M. F., & Fricke, K. J. 1985, *A&A*, 145, 179
- Langer, N., Wellstein, S., & Petrovic, J. 2003, in *IAU Symposium*, Vol. 212, *A Massive Star Odyssey: From Main Sequence to Supernova*, ed. K. van der Hucht, A. Herrero, & C. Esteban, 275
- Lau, H. H. B., Gil-Pons, P., Doherty, C., & Lattanzio, J. 2012, *A&A*, 542, A1
- Lecoanet, D., Schwab, J., Quataert, E., Bildsten, L., Timmes, F. X., Burns, K. J., Vasil, G. M., Oishi, J. S., & Brown, B. P. 2016, *ApJ*, 832, 71
- Maeder, A. 1976, *A&A*, 47, 389
- . 1987, *A&A*, 178, 159
- Manreza Paret, D., Horvath, J. E., & Perez Martínez, A. 2015, *Research in Astronomy and Astrophysics*, 15, 1735
- Marchant, P., Langer, N., Podsiadlowski, P., Tauris, T. M., & Moriya, T. J. 2016, *A&A*, 588, A50
- Miyaji, S. & Nomoto, K. 1987, *ApJ*, 318, 307
- Miyaji, S., Nomoto, K., Yokoi, K., & Sugimoto, D. 1980, *PASJ*, 32, 303
- Moriya, T. J. & Eldridge, J. J. 2016, *MNRAS*, 461, 2155
- Nomoto, K. 1984, *ApJ*, 277, 791
- . 1987, *ApJ*, 322, 206
- Packet, W. 1981, *A&A*, 102, 17
- Paczynski, B. 1971, *AcA*, 21, 271
- . 1991, *ApJ*, 370, 597
- Paxton, B., Bildsten, L., Dotter, A., Herwig, F., Lesaffre, P., & Timmes, F. 2011, *ApJS*, 192, 3
- Paxton, B., Cantiello, M., Arras, P., Bildsten, L., Brown, E. F., Dotter, A., Mankovich, C., Montgomery, M. H., Stello, D., Timmes, F. X., & Townsend, R. 2013, *ApJS*, 208, 4
- Paxton, B., Marchant, P., Schwab, J., Bauer, E. B., Bildsten, L., Cantiello, M., Dessart, L., Farmer, R., Hu, H., Langer, N., Townsend, R. H. D., Townsley, D. M., & Timmes, F. X. 2015, *ApJS*, 220, 15
- Podsiadlowski, P., Langer, N., Poelarends, A. J. T., Rappaport, S., Heger, A., & Pfahl, E. 2004, *ApJ*, 612, 1044
- Poelarends, A. J. T., Herwig, F., Langer, N., & Heger, A. 2008, *ApJ*, 675, 614
- Pols, O. R. 1994, *A&A*, 290, 119
- Popham, R. & Narayan, R. 1991, *ApJ*, 370, 604
- Reimers, D. 1975, *Memoires of the Societe Royale des Sciences de Liege*, 8, 369
- Ritossa, C., Garcia-Berro, E., & Iben, I. J. 1996, *ApJ*, 460, 489
- Ritossa, C., García-Berro, E., & Iben, I. J. 1999, *ApJ*, 515, 381
- Ritter, H. 1988, *A&A*, 202, 93
- Sana, H., de Koter, A., de Mink, S. E., Dunstall, P. R., Evans, C. J., Hénault-Brunet, V., Maíz Apellániz, J., Ramírez-Agudelo, O. H., Taylor, W. D., Walborn, N. R., Clark, J. S., Crowther, P. A., Herrero, A., Gieles, M., Langer, N., Lennon, D. J., & Vink, J. S. 2013, *A&A*, 550, A107
- Sana, H., de Mink, S. E., de Koter, A., Langer, N., Evans, C. J., Gieles, M., Gosset, E., Izzard, R. G., Le Bouquin, J.-B., & Schneider, F. R. N. 2012, *Science*, 337, 444
- Scalzo, R. A., Aldering, G., Antilogus, P., Aragon, C., Bailey, S., Baltay, C., Bongard, S., Buton, C., Childress, M., Chotard, N., Copin, Y., Fakhouri, H. K., Gal-Yam, A., Gangler, E., Hoyer, S., Kasliwal, M., Loken, S., Nugent, P., Pain, R., Pécontal, E., Pereira, R., Perlmutter, S., Rabinowitz, D., Rau, A., Rigaudier, G., Runge, K., Smadja, G., Tao, C., Thomas, R. C., Weaver, B., & Wu, C. 2010, *ApJ*, 713, 1073
- Schneider, F. R. N., Podsiadlowski, P., Langer, N., Castro, N., & Fossati, L. 2016, *MNRAS*, 457, 2355
- Schwab, J., Quataert, E., & Bildsten, L. 2015, *MNRAS*, 453, 1910
- Schwab, J., Quataert, E., & Kasen, D. 2016, *MNRAS*, 463, 3461
- Shao, Y. & Li, X.-D. 2014, *ApJ*, 796, 37
- Siess, L. 2006, *A&A*, 448, 717
- . 2007, *A&A*, 476, 893
- . 2010, *A&A*, 512, A10
- Subramanian, S. & Mukhopadhyay, B. 2015, *MNRAS*, 454, 752
- Takahashi, K., Yoshida, T., & Umeda, H. 2013, *ApJ*, 771, 28
- Taubenberger, S., Benetti, S., Childress, M., Pakmor, R., Hachinger, S., Mazzali, P. A., Stanishev, V., Elias-Rosa, N., Agnoletto, I., Bufano, F., Ergon, M., Harutyunyan, A., Inserra, C., Kankare, E., Kromer, M., Navasardyan, H., Nicolas, J., Pastorello, A., Prospero, E., Salgado, F., Sollerman, J., Stritzinger, M., Turatto, M., Valenti, S., & Hillebrandt, W. 2011, *MNRAS*, 412, 2735
- Tauris, T. M., Kramer, M., Freire, P. C. C., Wex, N., Janka, H.-T., Langer, N., Podsiadlowski, P., and Bozzo, E., Chaty, S., Kruckow, M. U., van den Heuvel, E. P. J., Antoniadis, J., Breton, R. P., & Champion, D. J. 2017, *ApJ*, 846, 170
- Tauris, T. M., Langer, N., Moriya, T. J., Podsiadlowski, P., Yoon, S.-C., & Blinnikov, S. I. 2013, *ApJL*, 778, L23
- Tauris, T. M., Langer, N., & Podsiadlowski, P. 2015, *MNRAS*, 451, 2123
- Tauris, T. M. & van den Heuvel, E. P. J. 2006, *Formation and evolution of compact stellar X-ray sources*, ed. W. H. G. Lewin & M. van der Klis (Cambridge, UK: Cambridge University Press), 623–665
- The LIGO Scientific Collaboration, the Virgo Collaboration, Abbott, B. P., Abbott, R., Abbott, T. D., Acernese, F., Ackley, K., Adams, C., Adams, T., Addesso, P., & et al. 2017a, *Phys. Rev. Lett.*, 119, 161101
- . 2017b, *ArXiv:astro-ph/1710.05838*
- van Rensbergen, W., De Greve, J. P., De Loore, C., & Mennekens, N. 2008, *A&A*, 487, 1129
- Wellstein, S. & Langer, N. 1999, *A&A*, 350, 148
- Wellstein, S., Langer, N., & Braun, H. 2001, *A&A*, 369, 939
- Woosley, S. E. & Heger, A. 2015, *ApJ*, 810, 34
- Woosley, S. E., Heger, A., & Weaver, T. A. 2002, *Reviews of Modern Physics*, 74, 1015
- Yoon, S.-C. & Cantiello, M. 2010, *ApJL*, 717, L62
- Zahn, J.-P. 1977, *A&A*, 57, 383
- Zapartas, E., de Mink, S. E., Izzard, R. G., Yoon, S.-C., Badenes, C., Göteborg, Y., de Koter, A., Neijssel, C. J., Renzo, M., Schootemeijer, A., & Shrotriya, T. S. 2017, *A&A*, 601, A29

APPENDIX

A. OVERSHOOTING, FAST SEMI-CONVECTION AND THE CRITICAL M_{CO} FOR NEON IGNITION

The models presented in this paper use the Ledoux criterion for determining convective boundaries, and a small amount of semi-convection, $\alpha_{\text{sm}} = 0.01$. In order to investigate the robustness of our results against differences in the treatment of convection, we calculated two sequences (similar to the ones presented in Sec. 4.2), one with a stronger semi-convection ($\alpha_{\text{sm}} = 1.0$) and the other using overshooting ($f_{\text{ov}} = 0.016$, in the context of the Schwarzschild criterion). In this way we are able to determine whether the critical mass for neon ignition (in this paper found to be $M_{\text{CO}} \approx 1.52 M_{\odot}$) shifts to higher or lower M_{CO} with different convection criteria.

Figure A1 shows these various sequences (including Binary Sequence A from Fig. 8), calculated with different treatments of convection. Each sequence was calculated with initial masses between $10.0 M_{\odot}$ and $15.5 M_{\odot}$, for a mass ratio of $q = 0.8$, a period of 10 days and a mass transfer efficiency, $\beta = 0.5$. The sequence with $\alpha_{\text{sm}} = 1.0$ is shown with yellow symbols, and the sequence with Schwarzschild with $f_{\text{ov}} = 0.016$ with blue symbols.

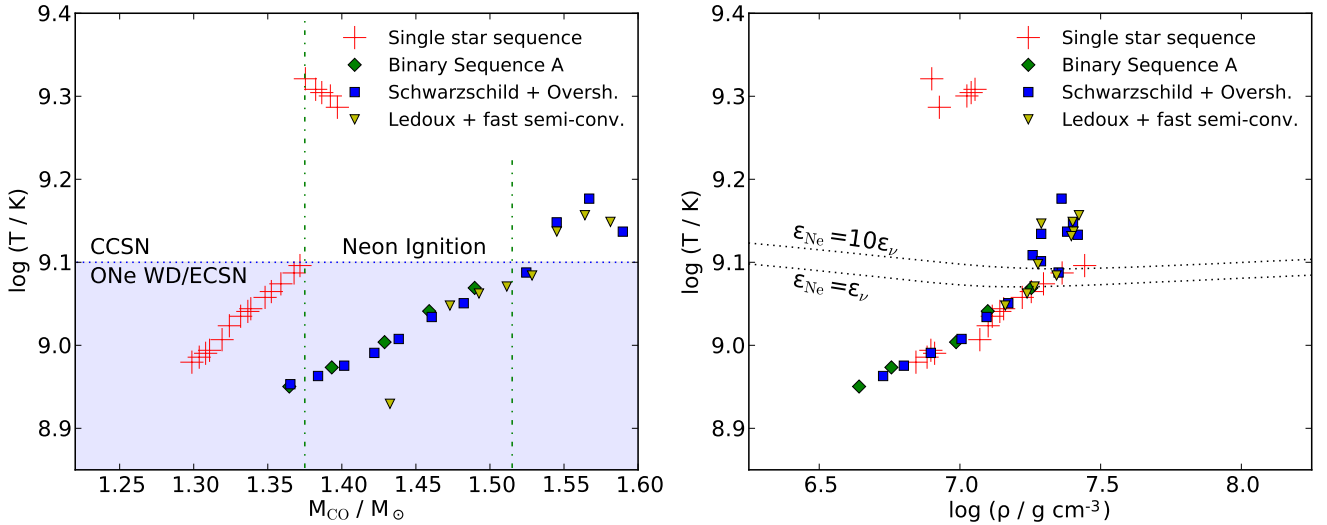


Figure A1. Maximum temperature attained in the core as a function of M_{CO} (left panel) and as a function of the density at the mass coordinate of T_{max} at the time of T_{max} (right panel), for single stars (red crosses) and primary stars in a binary system (filled symbols) with various treatments of convection and overshooting. The dotted line in the left panel approximates the critical temperature for neon ignition, while the dotted lines in the right panel give the locations where the energy generation of neon burning is equal to, and 10 times exceeds the energy losses due to thermal neutrinos.

While we defer a full investigation to a future work, this initial investigation shows that each of these modifications results in a relationship between M_{CO} and $\log T_{\text{max}}$ that is similar to the one shown in Fig. 8. This confirms that the critical mass for neon ignition in binary stars is not dependent on the adopted convection criterion, the efficiency of semi-convection, or the use of overshooting. However, each of these different modification does affect the initial mass range by shifting it to lower initial masses (c.f. Poelarends et al. 2008; Doherty et al. 2010).

B. THE EFFECTS OF VARIATION OF THE SPATIAL AND TEMPORAL RESOLUTION

As stellar models can potentially be quite sensitive to the spatial and temporal resolution, we conduct a small-grid resolution study to investigate the robustness of our models against spatial and temporal variations in resolution. While MESA has many parameters that control the temporal and spatial resolution in detail, the parameter w_t controls the overall temporal resolution, and the parameter δ_{mesh} controls the overall spatial resolution. The calculations described in this paper were computed with our baseline parameters $w_t = 9 \times 10^{-4}$ and $\delta_{\text{mesh}} = 0.8$. To investigate convergence of our models at a different resolution, we computed a sequence with $w_t = 9 \times 10^{-4}$ and $\delta_{\text{mesh}} = 0.3$ (increased spatial resolution), $w_t = 3 \times 10^{-4}$ and $\delta_{\text{mesh}} = 0.8$ (increased temporal resolution) and $w_t = 3 \times 10^{-4}$ and $\delta_{\text{mesh}} = 0.3$ (increased spatial and temporal resolution). The results are plotted in Fig. B2. The left panel shows the initial mass of the star versus the final M_{CO} , comparable to Fig. 13. The models with the baseline values are shown as green

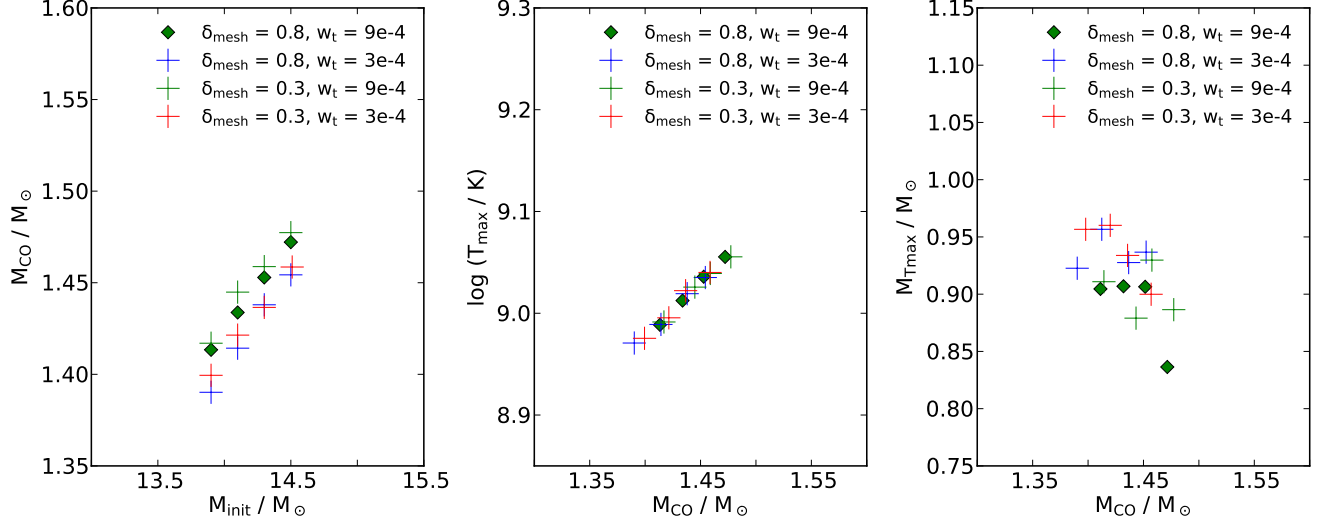


Figure B2. Results of our resolution study. Our baseline parameters are shown as green diamonds while variations in w_t and/or δ_{mesh} are shown with colored plus signs. The left panel shows the initial primary mass versus final CO core mass. The middle panel shows the CO core mass versus T_{max} , and the right panel shows the CO core mass versus the radial mass coordinate of T_{max} . All panel shows that our baseline models are within the convergence envelope and thus producing reliable results.

diamonds, while the variations in w_t and δ_{mesh} are shown with plus signs. A minimal spread can be seen in the resulting M_{CO} , with models with $w_t = 9 \times 10^{-4}$ slightly more massive than models with $w_t = 3 \times 10^{-4}$. The middle panel shows the maximum temperature attained in the core, plotted against the CO core mass (similar to Fig. 8). This panel shows excellent model convergence in the mass range considered, with no impact due to changes in spatial or temporal resolution. The location of T_{max} (shown in the far right panel) is a bit more sensitive to changes in the spatial and temporal resolution, but this can also be attributed to a steep relationship between M_{CO} and $M_{T_{\text{max}}}$ (c.f. Fig. C2 in Schwab et al. 2016). However, this variation has no impact on any of our results.

Based on this resolution study we conclude that our baseline parameters lead to good model convergence, and are comparable to models with a higher spatial and/or temporal resolution. The most notable difference is that our baseline models produce more massive cores than models with a higher spatial and temporal resolution. While this does not affect the relationship between the maximum temperature attained in the core and the CO core mass, a higher resolution grid would shift the initial mass range to higher initial primary masses.